# Electron-Ion Collider Detector Requirements and R&D Handbook

Version 1.2
February 25, 2020


**Authors**

Elke Aschenauer, Alexander Kiselev, Richard Petti, Thomas Ullrich, Craig Woody
Brookhaven National Laboratory, NY, US

Tanja Horn,
The Catholic University of America, Washington DC, US

Yulia Furletova,
Jefferson National Laboratory, VA, US

Pawel Nadel-Turonski
Stony Brook University, NY, US

Laura Gonella, Peter Jones
University of Birmingham, UK

Yordanka Ilieva
University of South Carolina, SC, US

Kondo Gnanvo
University of Virginia, VA, US

## Editors Notes

This handbook is a community effort. Many colleagues have made substantial and valuable contributions to this document and the studies it is based on. We consider this a living document that, as we hope, gets frequently updated and thus stays relevant for those that work on the realization of an EIC. EIC User Group members and those involved in the EIC detector R&D programs are invited to contribute to this document. If you want to contribute please send text (MS Word) and plots (preferably in eps format).

Alexander Kiselev
Thomas Ullrich


## Acknowledgements

The authors are indebted to the following colleagues for critical and crucial contribution and input in the preparation of this report:
M. Alfred, L. Allison, B. Azmoun, F. Barbosa, M. Boer, T. Cao, M. Chiu, I.J. Choi, E. Cisbani, M. Contalbrigo, A. Deldotto, S. Dalla Torre, M. Demarteau, A. Denisov, J.M. Durham, A. Durum, R. Dzhygadlo, C. Gleason, M. Grosse-Perdekamp, M. Hattawy, X. He, H. van Hecke, J. Huang, C. Hyde, G. Kalicy, B. Kim, E. Kistenev, M. Liu, J. McKisson, I. Mostafanezhad, K. Park, K. Peters, R. Pisani, W. Roh, M. Sarsour, C. Schwarz, J. Schwiening, C.L. da Silva, A. Sukhanov, X. Sun, S. Syed, R. Towell, G. Varner, R. Wagner, C.P. Wong, J. Xie, Z.W. Zhao, C. Zorn.

## Table of Contents


**1 INTRODUCTION ..... 5**

**2 MACHINE PARAMETERS ..... 7**

2.1 BEAM ENERGIES, LUMINOSITIES ..... 7

2.2 RATES AND MULTIPLICITY ..... 7

2.3 INTERACTION REGION ..... 9

**3 DETECTOR PERFORMANCE REQUIREMENTS ..... 12**

3.1 PHYSICS CONSIDERATIONS FOR DETECTOR DESIGN ..... 12

*3.1.1 Kinematics Overview ..... 13*

*3.1.2 Scattered Electrons ..... 14*

*3.1.3 Hadrons ..... 21*

*3.1.4 The Extreme Forward Region: Roman Pots ..... 22*

3.2 DETECTOR GOALS ..... 24

**4 TECHNOLOGIES AND R&D NEEDS ..... 27**

4.1 TRACKING SYSTEMS ..... 27

*4.1.1 Central Tracking ..... 27*

*4.1.2 Forwards and Backwards Tracking ..... 33*

*4.1.3 Roman Pots ..... 34*

*4.1.4 Low-Q2 Tagger ..... 37*

4.2 CALORIMETRY ..... 38

*4.2.1 Electromagnetic Calorimeters ..... 38*

*4.2.2 Hadron Calorimeters ..... 42*

*4.2.3 Zero Degree Calorimeter ..... 43*

4.3 PARTICLE ID ..... 43

*4.3.1 Hadron PID ..... 43*

*4.3.2 Electron identification ..... 44*

*4.3.3 Detector technologies ..... 45*

4.4 LUMINOSITY MEASUREMENTS ..... 51

4.5 TRIGGER AND DATA ACQUISITION ..... 52

4.6 POLARIZATION MEASUREMENTS ..... 52

*4.6.1 Electron Beam ..... 52*

*4.6.2 Proton Beam ..... 53*

*4.6.3 Light Ion Beams ..... 53*

**5 THE EIC R&D PROGRAM ..... 53**

**REFERENCES ..... 55**

# 1 Introduction

The 2015 Long Range Plan for Nuclear Science in the US recommends a high-energy high-luminosity polarized EIC as the highest priority for new facility construction following the completion of FRIB. The EIC will, for the first time, precisely image gluons in nucleons and nuclei. It will definitively reveal the origin of the nucleon spin and will explore a new quantum chromodynamics (QCD) frontier of ultra-dense gluon fields, with the potential to discover a new form of gluon matter predicted to be common to all nuclei. This science will be made possible by the EIC's unique capabilities for collisions of polarized electrons with polarized protons, polarized light ions, and heavy nuclei at high luminosity.

In line with this recommendation the LRP also emphasized that an EIC will require tools and techniques that are state-of-the-art or beyond and therefore recommends vigorous detector and accelerator R&D in support of the EIC.

The physics goals of the EIC will profit from advances in detector technology to optimize the physics outcome of the experiment(s). Improvements include reducing systematics to the lowest possible level in order to take advantage of the full luminosity for precision measurements and providing the best possible efficiencies and kinematic coverage. This document outlines the detector requirements and discusses the need for detector R&D that will allow us to meet these demands. It aims at describing the detector R&D envisaged for the timely construction of a detector with the required performance and to point out areas where efforts are missing or are inadequately covered.

Currently, R&D is conducted within a generic EIC detector R&D program supported through funds provided to BNL by the DOE Office of Nuclear Physics. It is not intended to be specific to any proposed EIC site and is open to all segments of the EIC community. Below we will also give a brief summary of the program and of the efforts pursued.

Although huge efforts were and are being made in detector development for the LHC program, with many benefits to detector technology, there are nevertheless significant differences to the demands of an EIC program. The principal challenges at the LHC are related to the high event rate and especially the high radiation levels associated with the *pp* energies and luminosities required to address the physics goals. Both of these problems are dramatically reduced at an EIC. The primary *new* requirements are (*i*) an unprecedented hermeticity to access the full $x, Q^2$ range and (*ii*) excellent tracking resolution and PID coverage over a wide range of momenta to achieve the highest precision. The latter requires, among other things, a very low material budget between the interaction point and the calorimeters. These challenges require R&D now to achieve the performance goals and to prepare for an optimal physics program at the EIC.
This document is structured as follows: In Section 2 we briefly summarize the machine parameters and emphasize the importance of the Interaction Region (IR) design and its impact on detector integration and design. Section 3 discusses the overall detector performance requirements driven by the physics program. In in Section 4 we review the actual R&D needs for the various detector components and in Section 5 we give a brief over-

view of the ongoing EIC R&D program. Here we do take into account the different detector designs under consideration and discuss the similarities and differences on R&D requirements.

# 2 Machine Parameters

The machine parameters were first discussed and largely defined at the 10-week INT program in Fall of 2010 [1]. Already at that point two substantial focused efforts at developing a design for an EIC were underway, one at BNL (eRHIC) and one at JLAB (JLEIC). Because both options are driven by the same science objectives, the two U.S. EIC design efforts have similar characteristics. The parameters were only slightly refined for the EIC White Paper [2] that was compiled in preparation for the NSA 2015 Long Range Plan process. Here we give the performance requirements and parameters as listed in the White Paper (version 2). Note that due to funding limitations and constructions costs, these parameters might not be reached at the beginning of EIC operations but only after a series of upgrades in a later stage of the program. Nevertheless, any detector design should be able to cope with the demands of the physics-driven requirements. While the energy of the specific beams drives the demands on the kinematic coverage for tracking and PID, the anticipated layout of the IR makes integration of the detector into the accelerator a particular challenge for any design.

## 2.1 Beam Energies, Luminosities

The EIC machine design parameters are:

- Highly polarized (~ 70%) electron and nucleon beams
- Ion beams from deuteron to the heaviest nuclei (uranium or lead)
- Variable center of mass energies from $\sqrt{s} \approx 20$ to 100 GeV, upgradable to ~140 GeV
- High collision luminosity of $\mathcal{L} \sim 10^{33\text{-}34}$ cm$^{-2}$ s$^{-1}$
- Possibilities of having more than one interaction region

Note that for heavy ions the center-of-mass energies have to be multiplied by $\sqrt{Z/A}$ of the respective ions. For Au ions this factor is ~0.63. The luminosity scales in good approximation with 1/A, although in most cases the quoted luminosity is given as *per nucleon* in which case the *ep* and *e*A values are identical.

The implications on the detector requirements are detailed in Section 3.

## 2.2 Rates and Multiplicity

For the desired energy range Table 1 lists the referring total *ep* cross-sections. The cross-sections were calculated using Pythia6 and should be regarded only as an approximation or ballpark figures. It is interesting to compare these cross-sections with the total inelastic pp cross-section at RHIC of ~42 mb at $\sqrt{s}$=200 GeV and that at the LHC of ~69 mb at $\sqrt{s}$=7 TeV. In the EIC range the Pythia cross-section can be approximated by the simple func-

tion: $\sigma_{tot}(\mu b) = 0.42 + 3.45 \log^2 s$, where $s$ is the square of the center-of-mass energy (in GeV$^2$) that is well approximated[1] by $s = 4\, E_e E_p$.

| $\sigma_{tot}$ (μb) | $E_e$ (GeV) | 5 | 10 | 15 | 20 |
|---|---|---|---|---|---|
| $E_p$ (GeV) | | | | | |
| 50 | | 31.4 | 38.0 | 42.1 | 45.3 |
| 100 | | 38.0 | 45.3 | 49.8 | 53.0 |
| 150 | | 42.2 | 49.8 | 54.1 | 57.8 |
| 200 | | 45.2 | 52.9 | 57.9 | 61.4 |
| 250 | | 47.8 | 55.5 | 60.6 | 64.4 |

*Table 1: Total ep cross-section as a function of electron and proton beam energies.*

From the cross-section one can easily estimate the approximate data rate at an EIC. For $\mathcal{L}$ = $10^{33}$ cm$^{-2}$ s$^{-1}$ = 1000 Hz/μb and a cross-section of 50 μb the total interaction rate is a moderate 50 kHz.

Figure 1 depicts the particle production rates as a function of pseudo-rapidity for 15 GeV on 250 GeV *ep* collisions at a luminosity of $\mathcal{L}$ = $10^{33}$ cm$^{-2}$ s$^{-1}$. Events were simulated using Pythia6. No cuts, for example on event $Q^2$ or particle momentum, were applied. "Charged" particles term refers to electrons, positrons, and charged pions and kaons, while "neutrals" refers to photons, neutrons and $K_L^0$.

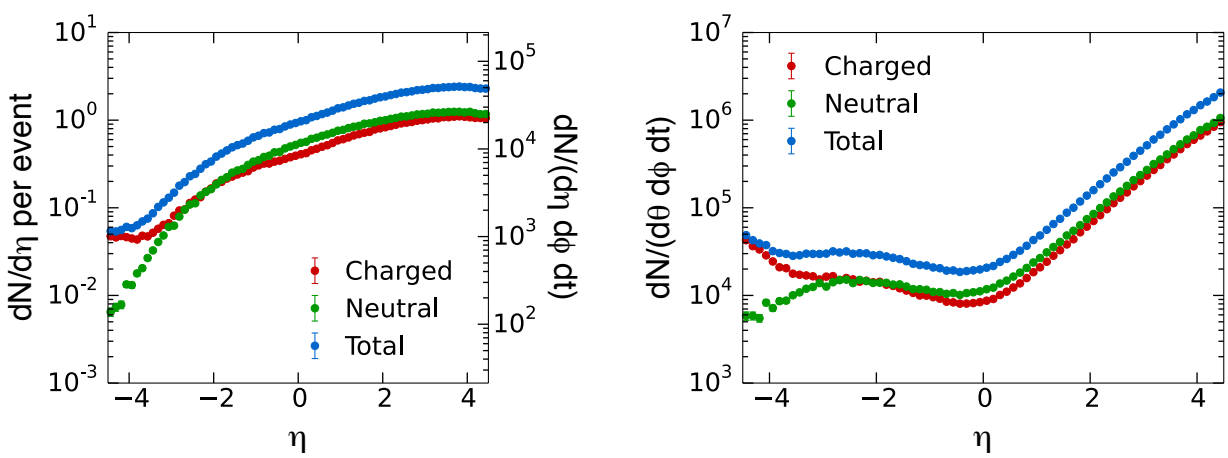


*Figure 1: Particle production rates as a function of pseudo-rapidity for 15 GeV on 250 GeV ep collisions and a luminosity of $10^{33}$ cm$^{-2}$ s$^{-1}$ . Left: Mean numbers of particles per event (left axis) and particles per second per unit (η, φ) (right axis). Right: Particles per second per unit (θ, φ) i.e. the η - dependent flux at a distance of 1m from the interaction point. Bending in the solenoid field is not accounted when building these plots.*

Overall the interaction rate as well as the multiplicity/occupancy in an EIC detector is rather small, especially when compared with RHIC or LHC conditions.

[1] In most kinematic calculation in this document the masses of electron and proton are neglected thus substantially simplifying any kinematic calculations.

## 2.3 Interaction Region

The IR design and proper interfacing of machine components in the detector installation area to the sub-detector systems, which are close to the beam line(s) is of a paramount importance for the success of the EIC physics program. In general, the ideal IR design is achieved when the accelerator is able to provide high luminosity collision events with minimal spread of the beam kinematic parameters and adverse effect on the rest of the physics detectors is minimal. This in particular implies that machine elements do not obscure the critically important parts of the acceptance, providing in particular a clear path to the auxiliary detectors installed tenth of meters away from the Interaction Point (IP). Where interference with the scattered tracks cannot be avoided, the adverse effects should be at a minimum. Machine-related backgrounds should be reduced to the lowest level possible.

Requirements and constraints, related to the IR design, come from various sources discussed throughout this document. They can be conventionally broken down into the following categories:

<u>Beam parameters at the IP:</u>
Reaching highest possible luminosity in general requires bringing the first focusing quads as close as possible to the IP. This implies the use of the strong focusing optics. Both requirements are in obvious conflict with the physics measurement. The former one inevitably obscures forward and backward acceptance once the beam line elements are "inserted" into the region primarily allocated for the main detector. This harms the registration of the low $Q^2$ scattered electrons and diffractive protons, respectively. The latter requirement causes unwanted (proton) beam divergence at the interaction vertex, which at a level of several hundred micro-radians negatively affects the $p_T$ reconstruction of diffractive scattered protons and, as simulations show, undermines the quality of the imaging data. Hadron bunch elongation beyond few centimeters would cause severe inefficiency in the vertex reconstruction procedure and in the scattered track parameter determination in general, as the reaction products start to miss a fraction of the vertex detector layers.

<u>Vacuum chamber and beam pipes:</u>
Several details of the vacuum system design at the IP are potentially in conflict with the requirements imposed by physics measurements. The beam pipe around the interaction vertex cannot be made infinitely thin (it is presently assumed to be 1mm thick Beryllium), and at the same time it cannot have too small a radius since the synchrotron fan produced by the incoming electron beam due to the bending in the upstream quads needs to pass through it unobstructed. This fact alone has obvious implications for vertex reconstruction, especially for low-momentum particles. Beam pipe sections can be connected to each other either by welding (which adversely affects the maintenance work in case beam pipe needs to be removed) or using relatively thick flanges, which can obscure the acceptance of the physics detector. There is most likely no space for the vacuum pumps in the detector installation region of the beam pipes, therefore most likely the NEG coating should be

used. However, this coating needs to be activated from time to time, which procedure implies beam pipe heating by up to 200 degree Celsius. It does not look feasible to disassemble the vacuum system every time for this type of maintenance work. Therefore, heating elements as well as the proper insulation required to protect the sensitive neighboring detectors (like silicon vertex tracker) must be most likely integrated into the beam pipe design. This, however, again increases both the material budget and the effective beam pipe radius.

Hadron-going direction:
It is assumed that the vacuum chamber and the vacuum pipe design at the IP provide a clear acceptance cone of ±4 mrad for the neutrons after nuclear break-up, see Figure 14. Modelling of diffractive processes shows that at the highest considered proton beam energy of ~250 GeV (eRHIC design) one requires an unobstructed acceptance cone of up to ±5mrad with respect to the outgoing hadron beam line direction for the close-to-beam-energy scattered protons, see Figure 13. This requirement extends up to the anticipated location of the Roman Pot stations, see section 4.1.3. At lower proton beam energies (as well as in the JLEIC case in general), the requirement on this angular acceptance is proportionally higher, up to 20 mrad or so. This can be achieved by installing tracking stations in the location of the first (weak) large acceptance dipole magnet right downstream of the central tracker in the hadron-going direction. Also a noticeably large momentum acceptance for the charged products of the nuclear break-up for a wide range of magnetic rigidities is needed.

Electron-going direction:
The two key detectors that need to be integrated into the design, are the low-$Q^2$ tagger and the luminosity monitor. The former detector, which would most likely comprise a set of small-scale trackers and an electromagnetic calorimeter, needs to have sufficient acceptance, unobstructed by the beam pipe and the synchrotron photon masks. It needs to be integrated with the first bending dipole downstream of the IP. The latter one, which will very likely be designed similar to the ZEUS luminosity monitor, requires an unobstructed path for the bremsstrahlung photons from the $ep \to ep\gamma$ reaction between the incoming hadron and the outgoing electron beam lines. This also implies sufficient space to install the dipole of the pair spectrometer as well as the photon and $e^+e^-$ conversion-pair calorimeters.

Machine-related backgrounds:
The major backgrounds directly related to the IR design are (*i*) the synchrotron fan produced by the electron beam when it passes through the final focusing quads right upstream of the central detector and (*ii*) the products of the beam-gas interaction, associated with the hadron beam. The former one requires careful design of the beam pipe system, with several masks along the way. However, it causes the unwanted beam pipe widening in the outgoing electron direction. The downstream masks cannot be installed too close to the main detector because of the synchrotron-photon back-scattering. The latter one can produce heavy hadronic background in the main detector correlated with the bunch crossings, due to the high enough proton-nucleus and nucleus-nucleus cross-sections, for the *ep*- and *e*A-running, respectively. These two sources of background are somewhat inter-

connected, since the beam pipe heating due to the synchrotron fan causes excessive out-gassing from its wall material, thus increasing the rate of the beam-gas interactions.

Other auxiliary detectors like beam position monitors and the polarimeters (for the proton and the light ion beams in particular) may also need to be installed close to the IP location. This will require additional integration efforts in this already very dense environment.

# 3 Detector Performance Requirements

## 3.1 Physics Considerations for Detector Design

In this document we use the coordinate system and the directions of the beams as defined for HERA at DESY. The hadron beam goes in the positive $z$ direction (0°) and the electron beam in the negative z-direction (180°) as indicated in Figure 2. Particles with a positive $p_z$ have positive values in pseudo-rapidity, $\eta > 0$, particles with $p_z < 0$ have negative pseudo-rapidity values. The acceptances of the various detector groups are only meant for illustration.

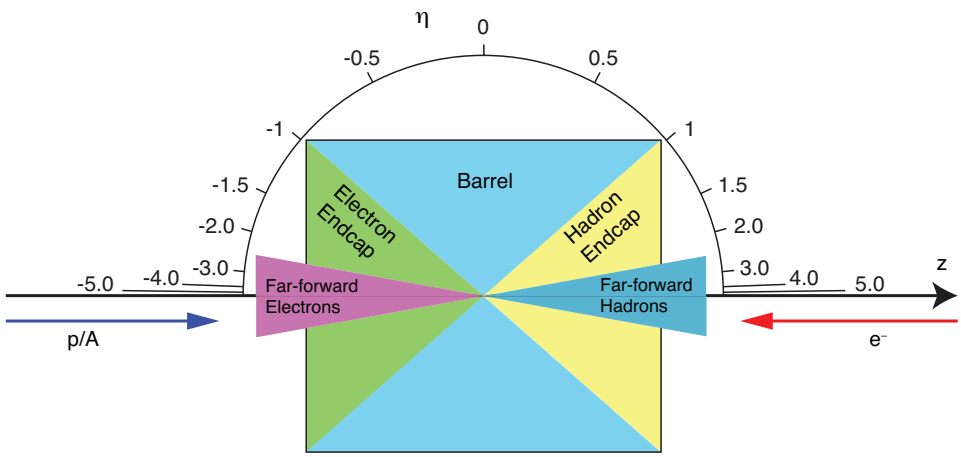


*Figure 2: Illustration of the reference frame used in this document*

In order to define the requirement for a EIC detector all relevant physics processes need to be considered. In the most general terms they encompass:

- Inclusive measurements ($ep/e\mathrm{A} \rightarrow e' + X$), which require either the detection of the scattered lepton or the full scattered hadronic debris with high precision (Jacquet-Blondel method, see sidebar) in order to extract $x$, $Q^2$, and $y$.
    - Physics: Structure Functions such as $g_1$, $F_2$, $F_L$
    - General requirements: Very good scattered electron ID and excellent energy/momentum and angular resolution of $e'$
- Semi-inclusive processes ($ep/e\mathrm{A} \rightarrow e' + h + X$) that require detection in coincidence with the scattered lepton of at least one (current or target fragmentation region) hadron, $h$.
    - Physics: TMDs, Helicity PDFs, FFs (with flavor separation), di-hadron correlations, Kaon asymmetries, multiplicities, etc.
    - General requirements: Excellent hadron ID, i.e., $\pi^{\pm}$, $K^{\pm}$, $p^{\pm}$ separation over a wide momentum and rapidity range, full φ-coverage around $\gamma^*$, wide $p_T$ coverage, excellent vertex resolution for charm, bottom separation.
- Exclusive processes, which require detection of all particles in the reaction.

- Physics: DVCS, exclusive (diffractive) VM production for GPDs and parton imaging in $b_T$.
- General requirements: Large rapidity coverage, high momentum resolution, wide coverage in $t = (p_{\mathrm{h,out}} - p_{\mathrm{h,in}})^2$ via Roman Pots, sufficient acceptance for neutrons in ZDC to detect breakup of nucleus in $e$A and determination/approximation of impact parameter of $e$A collision.

**Jacquet-Blondel and Mixed Methods**

In general, the key kinematic variables $x$, $Q^2$, and $y$ are derived from the momentum and angle of the scattered electron alone. However, at small scattering angles the resolution for the scattered lepton deteriorates. This problem is addressed by reconstructing the lepton kinematics purely from the hadronic final state using the Jacquet-Blondel [3] method or using a mixed method like the double angle method [4], which uses information from the scattered lepton and the hadronic final state. At HERA, these methods were successfully used down to $y$ of 0.005. The main reason this hadronic method renders better resolution at low y follows from the equation $x_{JB} = (E - p_z^{had})/E_e$, where $E - p_z^{had}$ is the sum over the energy minus the longitudinal momentum of all hadronic final-state particles and $E_e$ is the electron beam energy. This quantity has no degradation of resolution for $y < 0.1$ as compared to the electron method, where $y_{JB} = 1 - (1 - \cos\theta_e)E_{e'}/E_e$. To allow for efficient unfolding of measured quantities, i.e. cross sections and asymmetries, for smearing effects due to detector resolutions and radiative events and retain the statistical power it is important to have a survival probability in each kinematic bin of ~70% or better.

### 3.1.1 Kinematics Overview

Before going into details it is instructive to recall the kinematics of DIS in the $Q^2$-$x$ plane for $ep$ collisions. Shown in Figure 3 are the isolines of the scattered electron energy, i.e. the lines of constant energy, as well as the isolines of scattered electron pseudo-rapidity, i.e. lines of constant η. Here we can already note that low $x$/low-$Q^2$ physics is related to extremely forward going electrons at large rapidities, while for large $x$, large $Q^2$ processes we have to deal with back scattered electrons. Figure 4 shows a similar plot but for the isolines of the struck quark. In both figures a *narrow* spacing of isolines of a variable indicates that a variable is very sensitive to the kinematics of the collision and hence yields a good intrinsic resolution. The direction of the isolines determines to which kinematic parameter the variable is most sensitive. The actual resolution is a convolution of the intrinsic resolution of the reconstruction method and the experimental resolution of the measured quantities. From the isolines picture one can for example predict that the Jacquet-Blondel method yields a poor $Q^2$ determination over nearly the entire phase-space. The intrinsic resolution of $y_{JB}$ on the other hand is quite good as the $E_q$ isolines are dense and mostly parallel to the $y$ isolines. The $y$ determination from the electron method at low $y$ is nearly impossible because the electron energy is nearly constant over a very wide region of phase space. Conversely, we can exploit the wide spacing of $E_{e'}$ isolines to define a sample of

events that have a nearly constant scattered electron energy without actually measuring this energy.

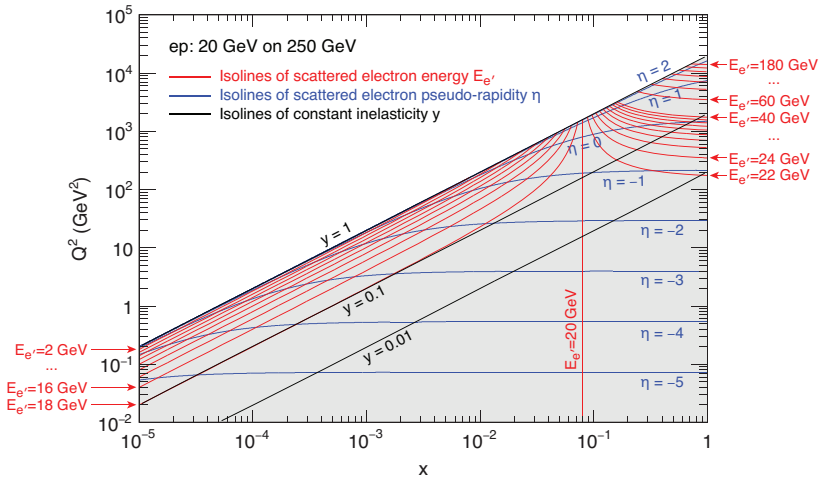


*Figure 3: Isolines of the scattered electron energy $E_{e'}$ and η for 20 GeV on 250 GeV ep collisions.*

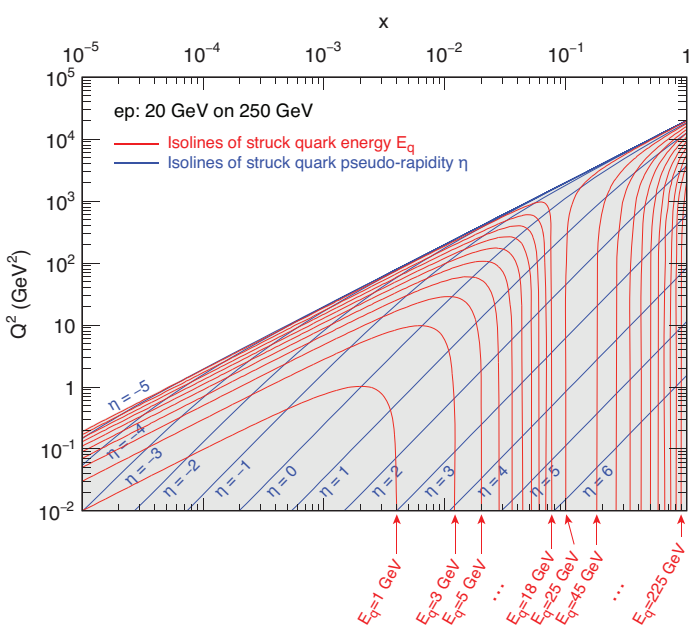


*Figure 4 : Isolines of the struck quark energy $E_q$ and pseudorapidity η for 20 GeV on 250 GeV ep collisions.*

### 3.1.2 Scattered Electrons

Figure 5 below, illustrates the kinematics of the scattered electron for various $Q^2$ ranges (integrated over all $x$), as well as differing beam energy combinations. The $z$-axes (color scale) in the plots reflects the cross-section, the distance from the center point denotes the momentum of the scattered electron and the directions reflects the actual one in the interaction. The events were produced with the Pythia6 generator.

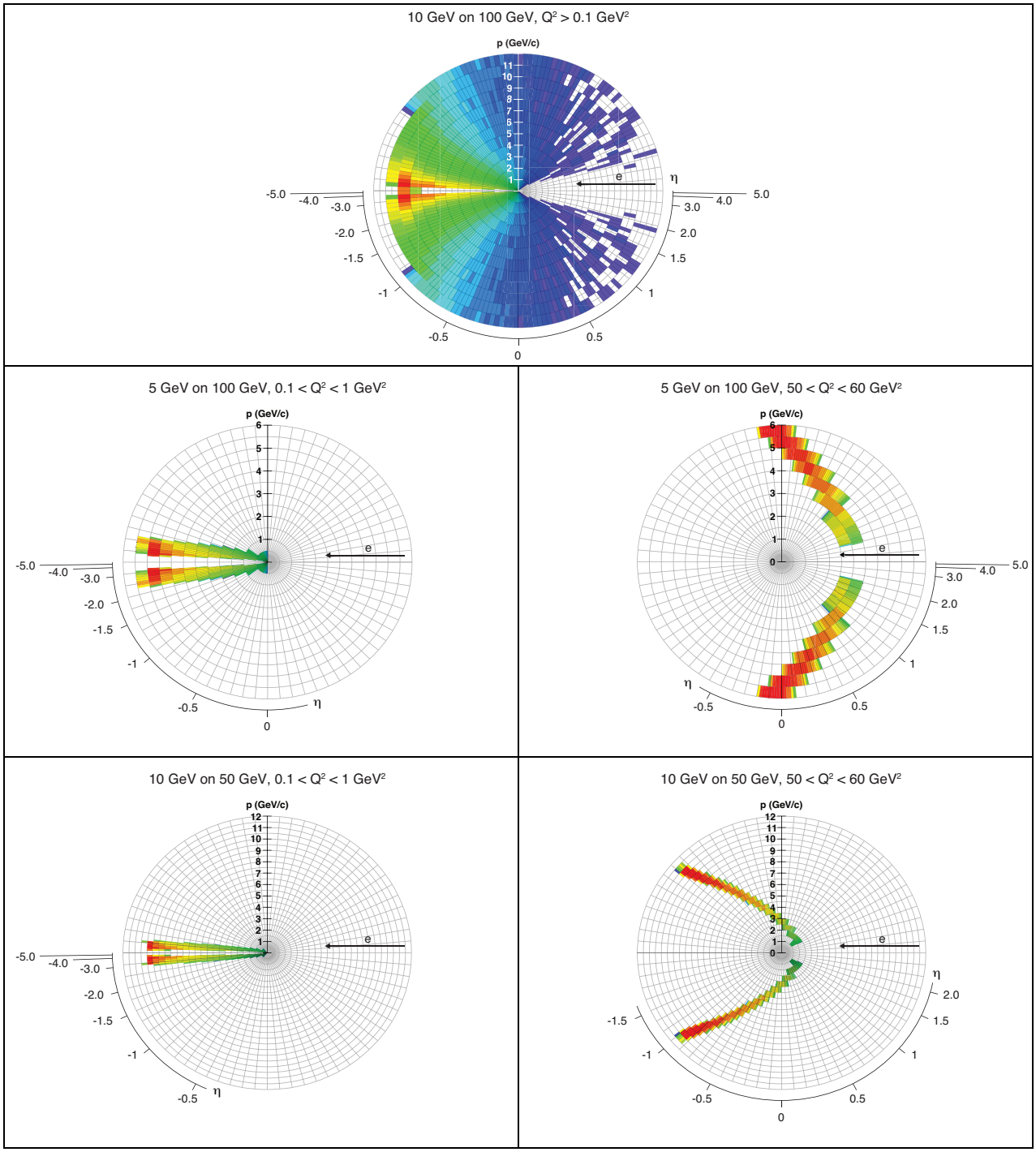

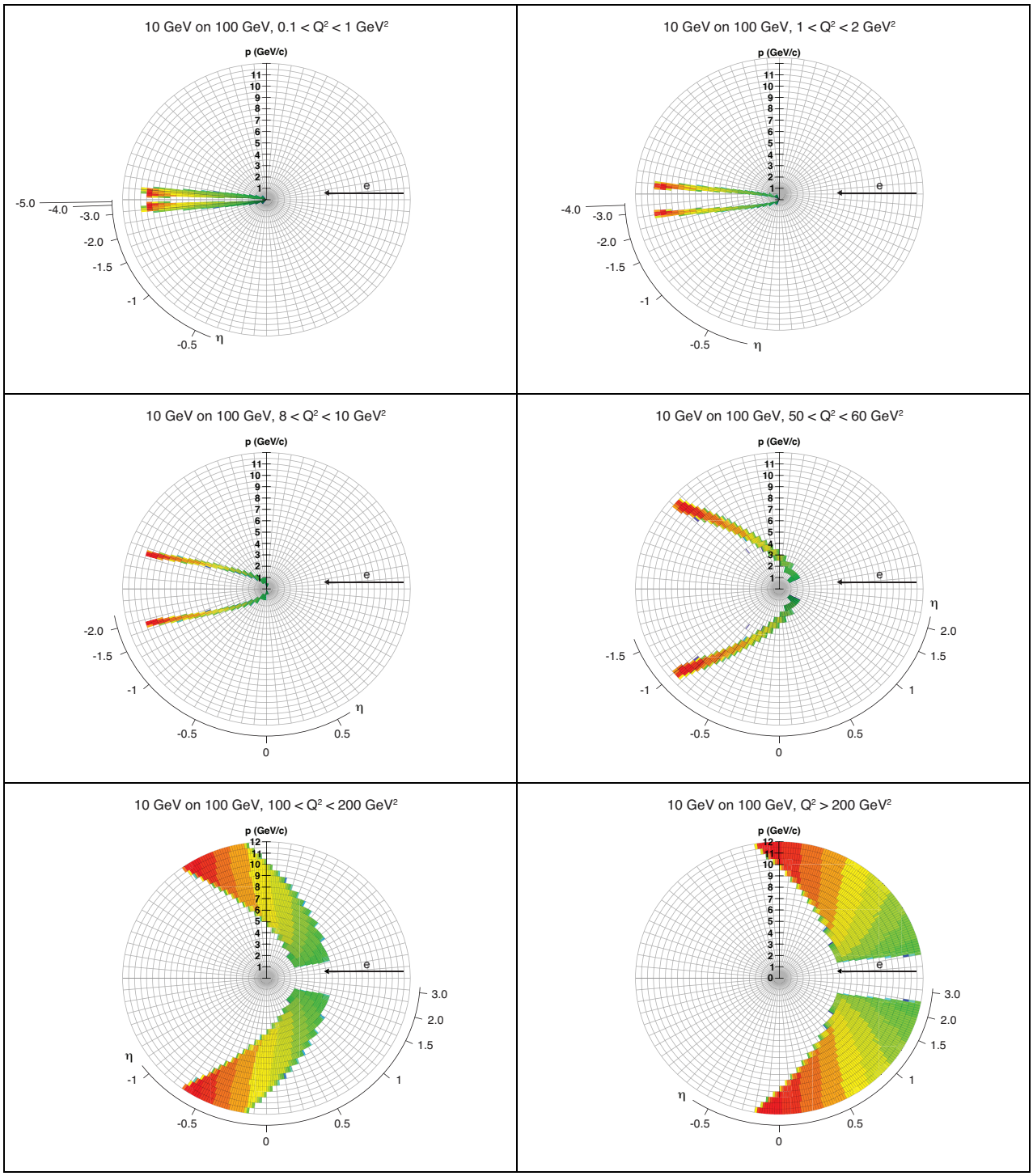
10 GeV on 100 GeV, 0.1 < Q² < 1 GeV²
10 GeV on 100 GeV, 1 < Q² < 2 GeV²
10 GeV on 100 GeV, 8 < Q² < 10 GeV²
10 GeV on 100 GeV, 50 < Q² < 60 GeV²
10 GeV on 100 GeV, 100 < Q² < 200 GeV²
10 GeV on 100 GeV, Q² > 200 GeV²
p (GeV/c)
η
e

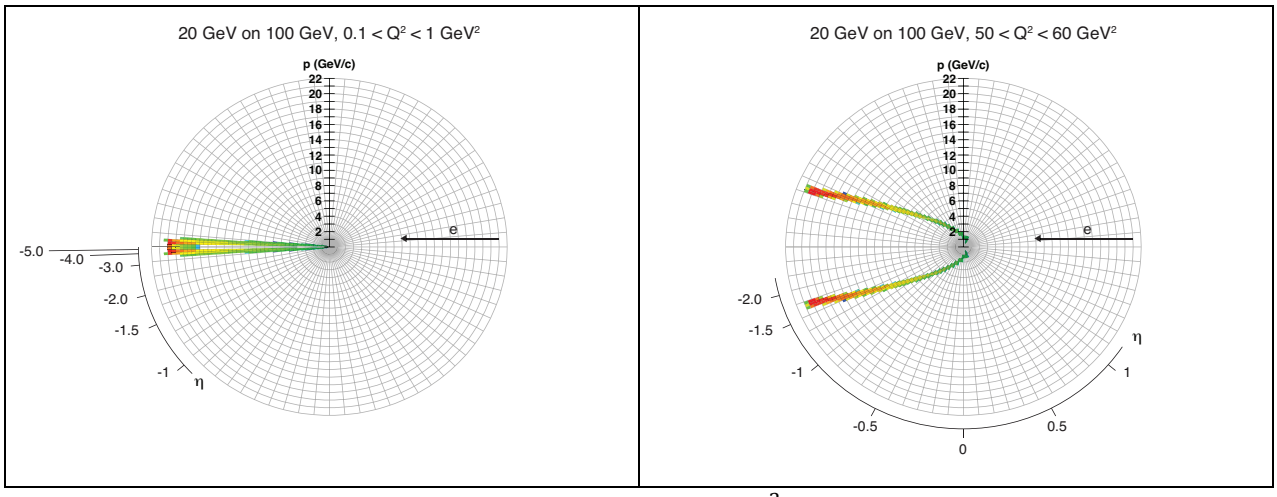


*Figure 5: Kinematic of the scattered electron for various $Q^2$ bins as well as different beam energy combinations. For details see text.*

A few things should be noted. At a given set of beam energies, the lower the $Q^2$ the more forward (negative η) the scattered electron goes. Only at the highest $Q^2$ does the scattered electron backscatter (positive η). Also notice that as the electron beam energy goes up the scattered electron is more and more boosted to negative η. Another important observation is that the kinematics of the electron does not change when varying the hadron beam energy. This has enormous consequences for the choice of beam energy combinations. For a detector that is optimized for electron measurements in a given range, in general it is often better to vary the hadron beam energy than the electron energy if measurements at a different $\sqrt{s}$ are desired. However, for certain semi-inclusive measurements it could be rather desirable to maintain *hadrons* in the similar kinematic conditions if these conditions are optimized for the hadron PID.

An alternative view of showing the $Q^2 - \eta$ relation is illustrated in Figure 6 for proton beam energy of 250 GeV and 10, 15, and 20 GeV electron beam energy.

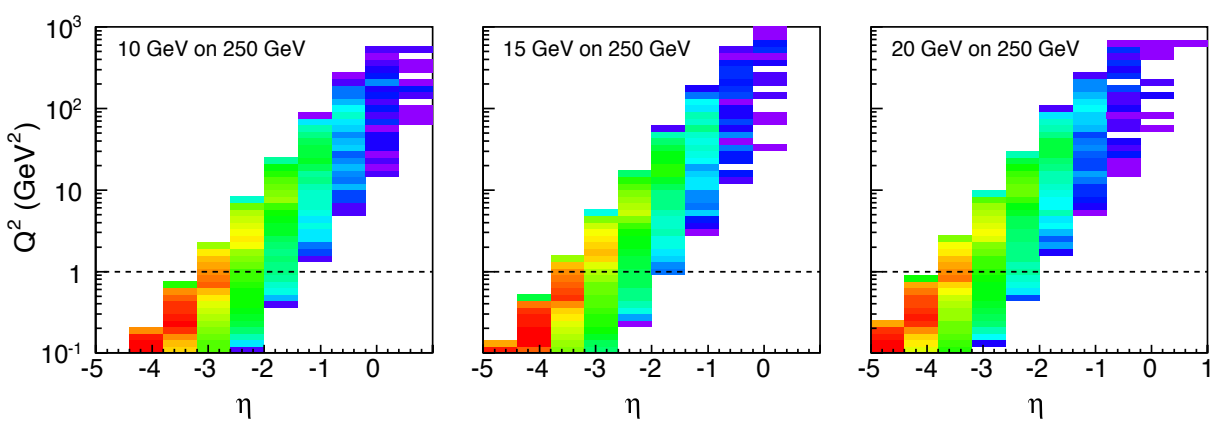


*Figure 6: Scattered electron $Q^2$, η for various electron beam energies and fixed hadron beam energy.*

It is also helpful to look at the kinematics of the scattered electron in bins of x and $Q^2$. Figure 7 shows the typical acceptance of an EIC in the $(x, Q^2)$ plane for $e$A collisions for √s=90 GeV and 45 GeV. The black boxes indicate the ranges of the following plots shown in Figure 8. Note that with the exception of area 5 (large $x$ and $Q^2$), the scattered electron travels close to the beamline; in the low $x$ region (areas 1 and 2), which is important for saturation physics and DVCS it scatters at extremely small angle $\eta$ < -3.

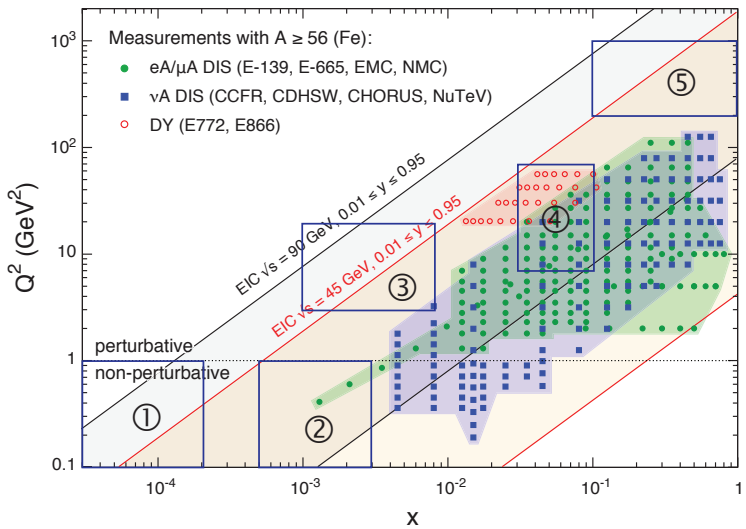


*Figure 7: EIC acceptance for eA collisions in the x, $Q^2$ plane. The black squares indicate the kinematic ranges of the figures below (Figure 8).*

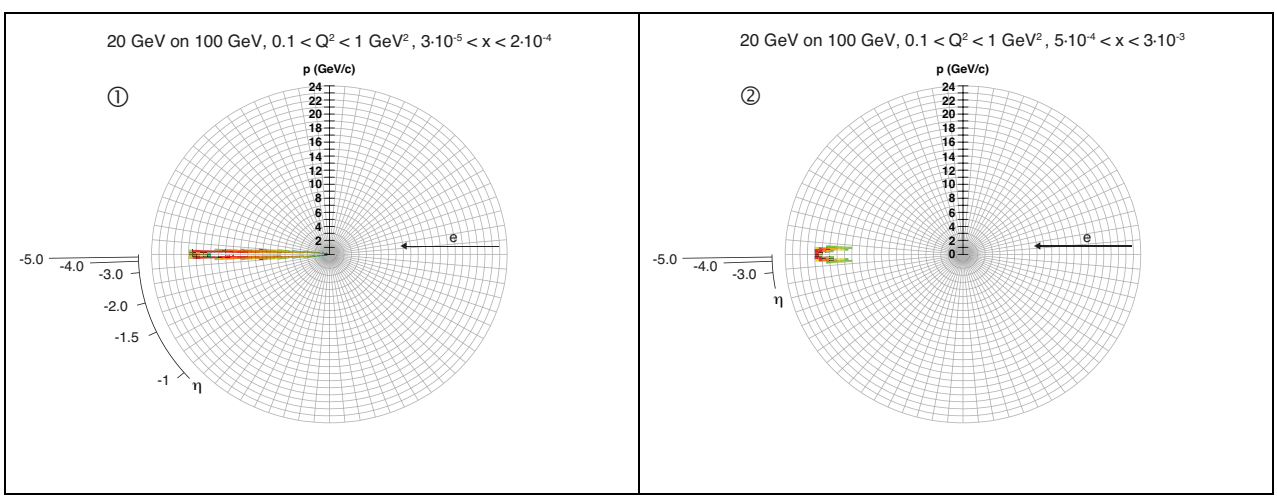

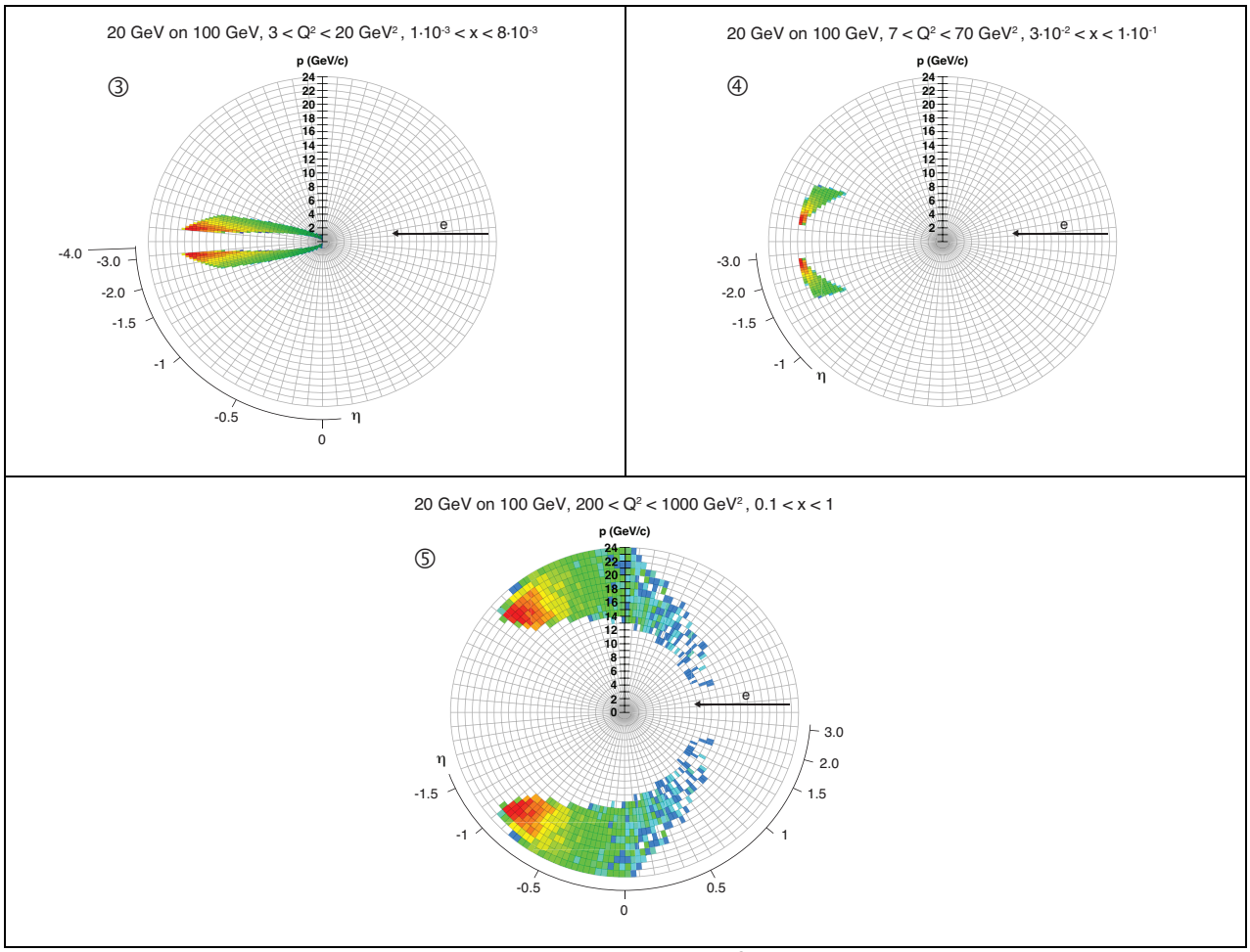


*Figure 8: Kinematic of the scattered electron for the x and $Q^2$ ranges indicated in Figure 7.*

For the detection of the scattered electron we conclude that for $Q^2 > 1.0$ GeV², a rapidity coverage $-4 < \eta < 1$ is sufficient, while for $Q^2 < 0.1$ GeV² a dedicated detector such as a low-$Q^2$ tagger is required.

Since electron ID most certainly does require electromagnetic calorimetry (EMC) it is useful to look at the Deep Virtual Compton Scattering (DVCS) process, $ep(A) \rightarrow e' + p'(A') + \gamma$, where the photon measurement does likewise require an EMC. Figure 9 shows the energy-rapidity relation of the photon. Note that increasing the hadron beam energy affects the maximum photon energy at a fixed η. From these results we conclude that a pseudo-rapidity coverage $-4 < \eta < 1$ is sufficient to capture the DVCS photon.

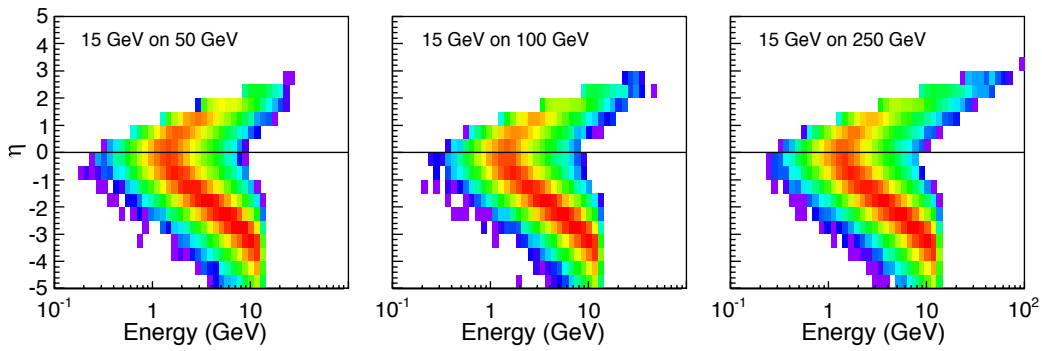


*Figure 9: Photon energy versus rapidity in DVCS processes for various hadron beam energies and fixed electron beam energy of 15 GeV. Plots are for $Q^2$ > 1 GeV, 0.01 < y <0.85.*

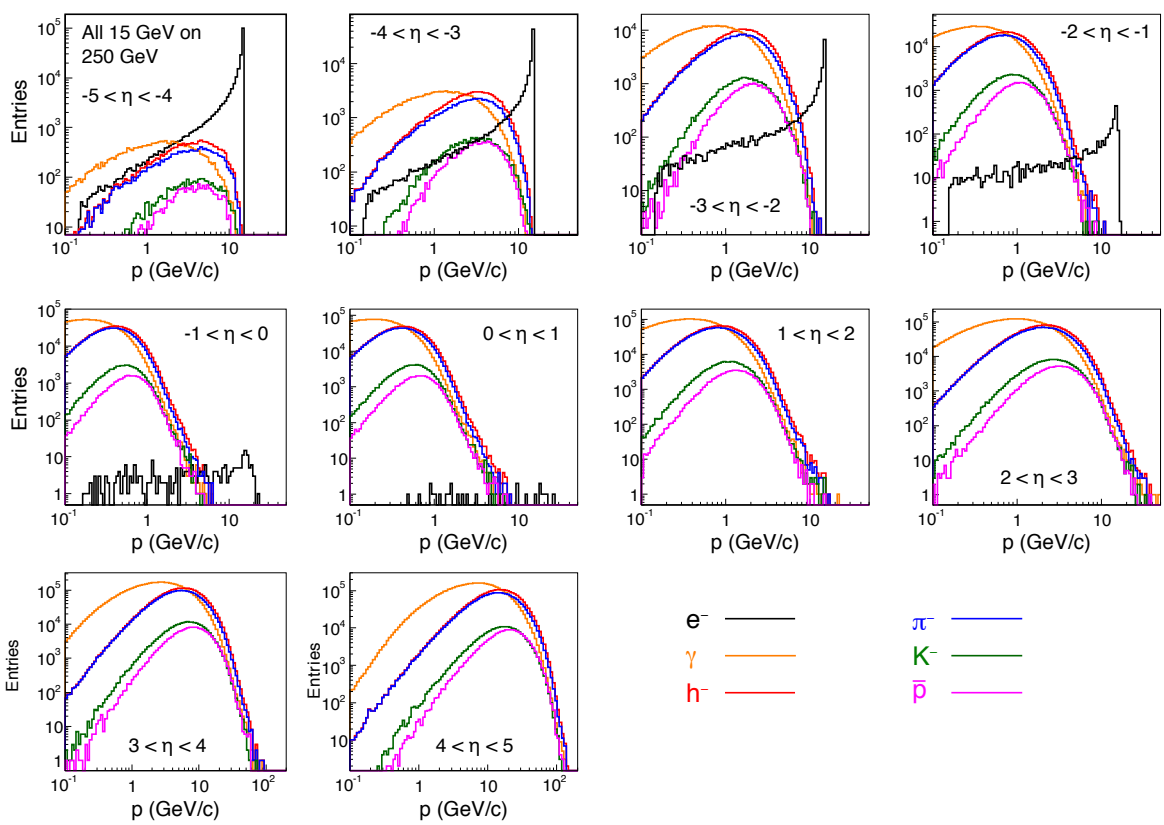


*Figure 10: Momentum distributions for the scattered electrons (black), photons (orange), all negatively charged hadrons (red) for different pseudo-rapidity bins in the laboratory frame for beam energies of 15 GeV on 250 GeV. Also shown are the distributions for negatively charged Pions (blue), Kaons (green) and antiprotons (violet). No kinematic cuts have been applied.*

### 3.1.3 Hadrons

We now turn to the requirement for hadrons. Figure 10 shows the relative yield of charged hadrons, and pions, kaons, and antiprotons in comparison to the scattered electron for various pseudo-rapidity bins for 15 GeV on 250 GeV *ep* collisions. For the entire pseudorapidity range shown here (-5 < η < 5) negative pions, kaons and antiprotons show the same momentum distributions, with negative pions having a factor ~3-5 higher multiplicity as negative kaons and antiprotons. In the central detector region (-1 < η < 1) the momenta are of typically 0.1 GeV/$c$ to 4 GeV/$c$ with a maximum of about 10 GeV/$c$.

We are now looking in more detail into the hadron kinematics using charged pions as an example. Figure 11 shows the η versus $p_T$ and η versus $z$ distribution for three different beam energy combinations: 15 GeV electron beam on 50, 100, and 250 GeV proton beam. It turns out that a range of -4 < $\eta$ < 3.5 covers almost the entire kinematic region in $p_T$ and $z$ that is important for physics.

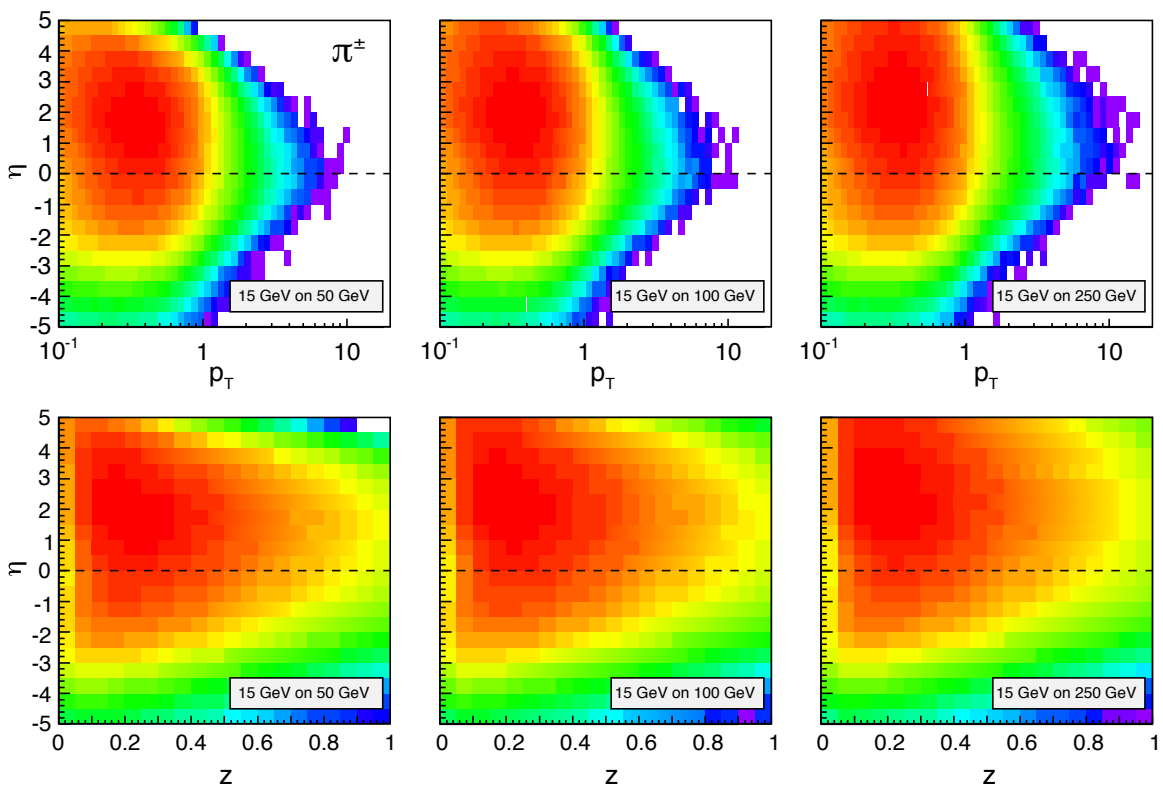


*Figure 11: Distribution of charged pions in $p_T$ and η (upper row) and z and η (lower row). Distributions are for ep collisions with fixed electron beam energy of 15 GeV and 50, 100, and 250 GeV proton beam energy. The following cuts have been applied: $Q^2$ > 1 GeV², 0.01 < y < 0.95, p > 1 GeV.*

Figure 12 shows the momentum versus pseudo-rapidity distribution for charged pions for different center-of-mass energies in *ep*. In the upper row the hadron beam energy is fixed at 250 GeV and the electron beam energy is varied from 10 to 20 GeV. In the lower row the

electron beam energy is fixed at 15 GeV and the proton beam energy is varied from 50 to 250 GeV. Two things should be noted: (*i*) When increasing the electron beam energy the hadrons are boosted more to negative rapidity, while (*ii*) increasing the hadron beam energy influences mostly the maximum hadron energy at a fixed pseudo-rapidity.

From Figure 12 one can conclude that in the $-2 < \eta < 3$ range $\pi/K/p$ separation below 5 GeV/$c$ should be sufficient. However, at large positive rapidities the requirements are rather challenging, demanding $\pi/K/p$ separation up to ~50 GeV/$c$.

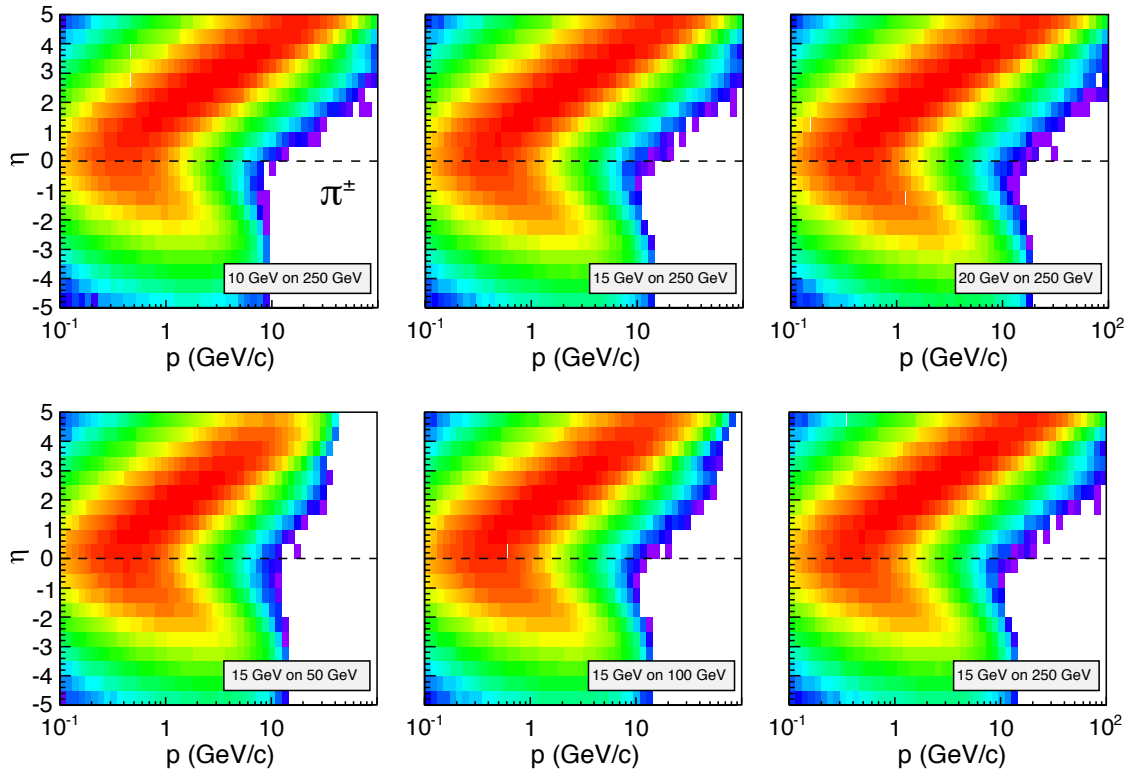


*Figure 12: Distribution of charged pions in p and η for 6 different beam energies. The following cuts have been applied: $Q^2 > 1$ GeV², $0.01 < y < 0.95$, $z > 0.1$.*

### 3.1.4 The Extreme Forward Region: Roman Pots

At the end of this section we discuss the need for the detection of forward-going scattered protons from exclusive reactions such as DVCS, as well as of decay neutrons from the breakup of heavy ions in non-diffractive reactions. In general, for exclusive reactions, one wishes to map the four-momentum transfer, $t$, of the hadronic system, and then obtain an image by a Fourier transform, for $t$ close to its kinematic limit up to about 1.5 GeV². One of the most challenging constraints for the interaction region and detector design from exclusive reactions is the need to detect the full hadronic final state.

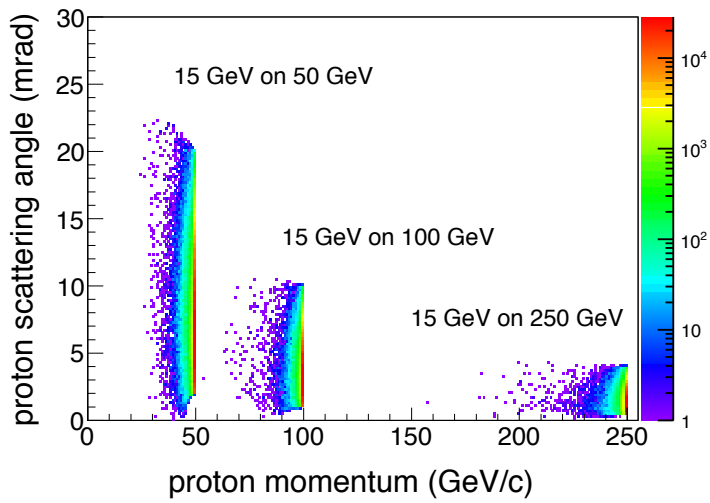


*Figure 13: The scattering angle vs. scattered proton momentum in the laboratory frame for DVCS events with different beam energy combinations. The following cuts have been applied: 1 GeV$^2$ < $Q^2$ < 100 GeV$^2$, 0.01 < $y$ < 0.85, $10^{-5}$ <$x$ <0.5 and 0.01 < $t$ < 1 GeV$^2$. The angle of the recoiling hadronic system is directly and inversely correlated with the proton energy. It thus decreases with increasing proton energy.*

Figure 13 shows the correlation between proton scattering angle in diffractive *ep* events ($e + p \rightarrow e' + p' + X$), and its momentum. It illustrates that the remaining baryonic states go in the very forward ion direction. Even at the proton energy of 50 GeV, the proton scattering angles only range to about 25 mrad. At proton energies of 250 GeV, this number is reduced to 5 mrad. In all cases, the scattering angles are small. Because of this, the detection of these protons is extremely dependent on the exact interaction region design. At present it is anticipated that the protons scattered in the ~5 mrad cone around the hadron beam direction should be detected by a Roman Pot system few tenths of meters away from the IP. Above ~5 mrad a set of tracking stations in the location of the first (weak) bending magnet in the outgoing hadron direction should be used.

One of the big challenges in measuring diffractive events in *e*A collisions is, apart from detecting the rapidity gap itself, to be able to distinguish between coherent (nucleus stays intact) and incoherent (nucleus decays). The only possible way ensuring exclusivity for electron-nucleus collisions for heavy nuclei is to veto the nuclear break up. This is realized by requiring no decay-neutrons in the hadron-going direction. How efficient this can be done depends on the angular acceptance of a neutron-detecting device such as a Zero-Degree Calorimeter (ZDC) as well as the emittance of the beam. Figure 14 shows the results of simulation using the diffractive event generator Sartre [5] in conjunction with the nuclear breakup generator Gemini++. Plotted is the inefficiency to tag an incoherent diffractive event as a function of the angular acceptance for neutron detection for 50 GeV Au and 100 GeV Al beams. A normalized emittance $\varepsilon_N = 0.2\times10^{-6}$ m and $\beta^* = 5$ cm were used. The inefficiency levels out and reaches a plateau when all decay neutrons are captured in the acceptance of the ZDC. The magnitude of the plateau is due to the lack of neutron emission at very low $t$ (where in fact it is less relevant because the coherent events dominate

the diffractive cross-section). The figure shows that the desired angular acceptance of a ZDC should be around ±4 mrad.

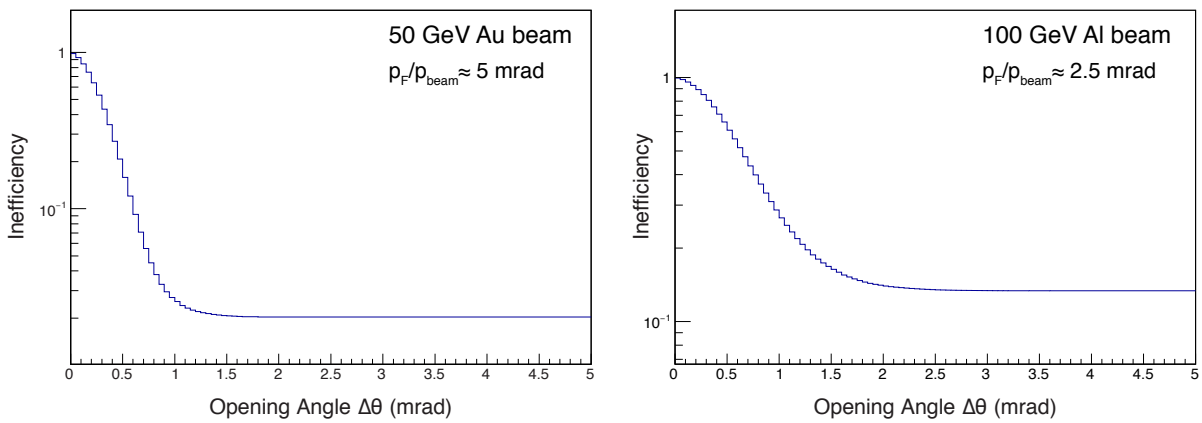


*Figure 14: Inefficiency to detect a neutron from a nuclear breakup in diffractive eA collision as a function of the angular acceptance of a neutron detecting device such as a Zero-Degree-Calorimeter (ZDC) for 50 GeV Au and 100 GeV Al beams. For details see text.*

Studies [6] showed that in SIDIS, collision geometries in *e*A can be determined by utilizing the ZDC since the number of forward neutrons produced and detected in the ZDC is sensitive to the path length of the parton and fragmentation of the colliding nucleon along the virtual photon direction in the nucleus. Also here, a considerably large ZDC acceptance is mandatory. It is anticipated at present that a ~10 interaction lengths sandwich-ZDC with transverse size of ~60x60 cm$^2$ and internal composition similar to the one developed for STAR forward upgrade [7] will be sufficient.

## 3.2 Detector Goals

In the previous section we listed the requirements that can be derived from the key physics measurements at an EIC in terms of rapidity coverage, momentum reach, and electron, photon, and hadron identification. What evolves is a detector with the following key features:

- Hermetic coverage, close to 4π acceptance (pseudo-rapidity range up to ±4)
- Low material budget on the level of 3-5% of $X/X_0$ for the central tracker region
- Tracking momentum resolution in few % range
- Reliable electron ID
- Good π/K/p separation in forward direction up to ~50 GeV/$c$
- High spatial resolution of primary vertex on the level of <20 microns

Other requirements can be derived from experiences at HERA and, to some degree, from LHC experiments. Table 2 summarizes all requirements as a function of pseudo-rapidity.

They are essentially identical for JLEIC and eRHIC machine designs. How these requirements are met and with what potential technologies is subject of the next chapter.

## EIC Detector Requirements

| η | Nomenclature | | | Tracking | | | Electrons | | π/K/p PID | | HCAL | Muons |
|---|---|---|---|---|---|---|---|---|---|---|---|---|
| | | | | Resolution | Allowed $X/X_0$ | Si-Vertex | Resolution $\sigma_E/E$ | PID | p-Range (GeV/c) | Separation | Resolution $\sigma_E/E$ | |
| -6.9 — -5.8 | ↓ p/A | Auxiliary Detectors | low-$Q^2$ tagger | $\delta\theta/\theta < 1.5\%$; $10^{-6} < Q^2 < 10^{-2}$ GeV$^2$ | | | | | | | | |
| … | | | | | | | | | | | | |
| -4.5 — -4.0 | | | Instrumentation to separate charged particles from photons | | | | 2%/√E | | | | | |
| -4.0 — -3.5 | | | | | | | | | | | | |
| -3.5 — -3.0 | | Central Detector | Backwards Detectors | $\sigma_p/p \sim 0.1\% \times p + 2.0\%$ | ~5% or less | TBD | | π suppression up to 1:$10^4$ | ≤ 7 GeV/c | ≥ 3σ | ~50%/√E | |
| -3.0 — -2.5 | | | | | | | | | | | | |
| -2.5 — -2.0 | | | | $\sigma_p/p \sim 0.05\% \times p + 1.0\%$ | | | | | | | | |
| -2.0 — -1.5 | | | | | | | 7%/√E | | | | | |
| -1.5 — -1.0 | | | | | | | | | | | | |
| -1.0 — -0.5 | | | Barrel | $\sigma_p/p \sim 0.05\% \times p + 0.5\%$ | | $\sigma_{xyz} \sim 20$ μm, $d_0(z) \sim d_0(r\phi) \sim 20/p_T$ GeV μm + 5 μm | (10-12)%/√E | | ≤ 5 GeV/c | | TBD | TBD |
| -0.5 — 0.0 | | | | | | | | | | | | |
| 0.0 — 0.5 | | | | | | | | | | | | |
| 0.5 — 1.0 | | | | | | | | | | | | |
| 1.0 — 1.5 | | | Forward Detectors | $\sigma_p/p \sim 0.05\% \times p + 1.0\%$ | | TBD | | | ≤ 8 GeV/c | | ~50%/√E | |
| 1.5 — 2.0 | | | | | | | | | | | | |
| 2.0 — 2.5 | | | | | | | | | ≤ 20 GeV/c | | | |
| 2.5 — 3.0 | | | | $\sigma_p/p \sim 0.1\% \times p + 2.0\%$ | | | | | | | | |
| 3.0 — 3.5 | | | | | | | | | ≤ 45 GeV/c | | | |
| 3.5 — 4.0 | ↑e | Auxiliary Detectors | Instrumentation to separate charged particles from photons | | | | | | | | | |
| 4.0 — 4.5 | | | | | | | | | | | | |
| … | | | | | | | | | | | | |
| > 6.2 | | | Proton Spectrometer | $\sigma_{intrinsic}(\lvert t\rvert)/\lvert t\rvert < 1\%$; Acceptance: $0.2 < p_T < 1.2$ GeV/c | | | | | | | | |

*Table 2: Physics requirements for a an EIC detector*

# 4 Technologies and R&D Needs

The majority of R&D in HEP and HENP is currently related to LHC phase-I (ALICE and LHCb) and phase-II upgrades (ATLAS, CMS). Here radiation hardness and high-rate capabilities are the top R&D priorities especially for pp collisions in the high-luminosity LHC era. Less emphasis is put on PID with the notable exceptions of the LHCb RICH (and TORCH upgrade) systems. Several R&D efforts related to phase-I such as MAPS Si-Sensors, RICH PID, and GEM based TPC readouts have by now concluded since the detectors are now being constructed.

As illustrated in the previous sections many requirements for an EIC are unique and therefore demand R&D that is not covered by the current mainstream HEP and HENP R&D efforts. In the following we discuss the possible technologies that could be deployed and to what extent R&D is necessary to make these technologies available for an EIC detector.

## 4.1 Tracking Systems

### 4.1.1 Central Tracking

#### 4.1.1.1 Main Tracker

The tasks of the main tracker are (i) to allow for highly efficient track finding of charged particles scattered at central rapidities, (ii) precise determination of particle kinematics (momenta and scattering angles) and, to the extent particular technology allows, (iii) participation in lepton and hadron PID as well as (iv) providing rough timing information (optionally). Unlike the LHC detectors the tracker should have very small overall material budget, on the level of a few % of the radiation length. It should fulfil the basic requirements in terms of redundancy, in particular provide sufficient number of independent measurements per track (in the order of few to several dozens of space points as anticipated presently, although the detailed track finding efficiency studies have not been performed yet). Since the EIC physics community clearly expressed its interest in **two** independent general-purpose EIC detectors, the tracking R&D program should identify more than one viable technology for the main tracker. For various reasons, depending on the choice of a particular technology (long enough lever arm for track fitting, efficient multiple track separation, sufficient number of points for $dE/dx$ measurement), but also because of the limited space inside an affordable (or readily available) solenoid magnet, a typical size of the main tracker is determined to be around 2 m in length and up to 80 cm in outer radius. The inner radius should be sufficient to accommodate the vertex detector. In case of an all-silicon main tracker the vertex and the main tracker are combined. The options considered so far are:

- <u>(A) Medium size TPC:</u> design either similar or identical to the sPHENIX central tracker. Moderate spatial resolution, somewhat compensated by the large number of independent measurement points for each track (sPHENIX design specs are 200-250 μm per space point and up to 40 points per track). If needed one can possibly improve both parameters significantly for an EIC application. For example ILC R&D

is targeted at obtaining better than 100 μm resolution per point in the whole volume, even for a much larger TPC; also one can most likely double the number of pad rows as long as the electronics costs are acceptable. Detector conveniently provides 3D points for tracking with no ambiguities, as well as a limited momentum range particle ID via $dE/dx$ measurement. Calibration procedure however may be cumbersome, especially at higher luminosities in the presence of large space charge distortions due to the high ion back flow. Ion back flow can be reduced drastically by a proper choice of gas mixture and operating voltage, but typically at a cost of significant deterioration of the $dE/dx$ resolution. This type of detector will suffer from a pile-up effects since the ionization produced by tracks from several bunch crossings is simultaneously present in the gas volume, due to the limited electron drift velocity (of an order of 30-80 μm/ns, which can result in a total drift time from the central membrane to the readout plane of up to ~30μs). This may or may not adversely affect track finding and track-to-event association procedures in the event reconstruction, given the relatively low charged track multiplicities of typical DIS events (of an order of one charged track per unit of pseudo-rapidity).

- <u>(B) Straw tubes:</u> design similar to the PANDA central tracker. High enough 1D spatial resolution in the radial-to-wire direction, typically better than 150 μm averaged over the tube volume, plagued however by the left-right ambiguity similar to the drift chambers. Spatial resolution in the direction along the wires can be provided by measuring time difference of signals arriving to both ends and is in general rather poor, in the order of ~1cm. Detector stacks of several layers can be designed with individual layers installed at small stereo angles to each other (few degrees), in order to provide the coarse coordinate measurement along the beam line also from the skewed UV-coordinate system. The adverse effect in this case is significant gaps between layers (so lower geometric efficiency) due to the fact that layer "container volumes" are no longer cylindrical but rather hyperbolic once the stack is glued together. Detector can be used with at least 1 bar over the atmospheric pressure (which means better $dE/dx$ due to the higher ionization per track unit length). In the over-pressure mode the detector is self-supporting. Short drift length means the detector is in general fast and with appropriate electronics one can use cluster counting technique for improved $dE/dx$ measurement.

- <u>(C) Drift chamber:</u> design similar to the ZEUS central tracker. Depending on the drift cell design (with the cells in general oriented along the beam line) the detector can have basic tracking properties similar to the straw tube tracker: decent 1D resolution and fast response, but poor resolution along the wires, and left-right ambiguity. Operational properties of the drift chamber solution are of a certain concern, since depending on the design details one broken wire may cause shutting down of a whole chamber segment.

- <u>(D) All-silicon detector:</u> this option would be a compact all silicon detector, made of vertex and tracking detector (see 4.1.1.2), main tracker and forward and backward trackers (see 4.1.2). Different parts of the detector would have to be optimized dif-

ferently. The main tracker could be equipped either with pixel or strip detectors. In case of pixel detectors, a monolithic solution, such as the DMAPS technology described in 4.1.1.2, would provide smaller pixels and lower material, and be more cost effective than hybrid pixel detectors. At present time, DMAPS and strip detectors can provide spatial resolution down to a few μm, and time resolution in the order of few tens of ns. A potentially interesting technology to monitor for use in an EIC main tracker would be fast timing detectors. State-of-the-art developments for the ATLAS HGTD based on LGAD sensors and dedicated readout ASIC can achieve time resolution of the order of tens of ps [8]. Technically the picosecond level timing allows such detectors to provide – at least in theory – very reasonable PID for up to a few GeV/$c$ momentum particles, even for very short, of an order of 1m, flight path. At the moment, however these detectors feature a pixel pitch in the order of a mm and have a large power consumption (1.3 mm and <300mW/cm$^2$ for the ATLAS HGTD[8]), which makes them unsuitable for operation at an EIC. Should developments in this technology progress towards reducing pixel size and optimize the electronics design to low power consumption, this would be an interesting option to add PID to a silicon main tracker.

- <u>(E) Micromegas tracker:</u> design similar to the CLAS12 tracker. Several concentric micromegas cylinders composed of the "curved tile" building blocks cover all the radial space between ~20 cm and ~80 cm. Such a detector can provide decent 1D coordinate measurement of an order of ~100 μm in both tangential direction (C-layer) and along the beam line (Z-layer). The configuration with stereo layers must be possible as well but more R&D is required to prove this. This solution will also most likely provide less than 10 points per track. Vigorous R&D is also needed to explore the double side MPGDs option that would double the number of points per track at a minimum cost for material budget. It is anticipated that detector operation in the so-called micro-drift mode must be possible. This could provide short "tracklet" seeds for the track finder rather than "single point" measurements as well as improved $dE/dx$ performance. The performance of micromegas in micro-drift mode may suffer from the strong solenoid magnetic field.

Depending on the details of the particular design the material budget of all these solutions can be sufficiently small, well below 10% radiation length. This may come at a cost of performance for options (B), (D) and (E), since in general both the tracker resolution and the material budget will scale with the number of layers. Reducing the number of tracking layers is only possible up to the point when track finding efficiency will start degrading, which is in particular true for the micromegas option and for the all-silicon tracker in case of 1D strip implementation.

One can seemingly achieve the required performance level in terms of momentum resolution with any of the options above, although the detailed Monte-Carlo studies have been performed only for the configurations (A), (D) and (E).

A slow "volume tracker" like a TPC can be complemented at the inner and the outer radius by few cylindrical Micro Pattern Gaseous Detector (MPGDs) layers of fast 2D tracking devices with spatial resolution better than 100 μm, which would provide seed tracks correlated with the bunch crossing as well as serve the purpose of TPC calibration. Prime candidate technology for this would be cylindrical micromegas (see above), but the more modern μRWELL option may be considered as well. Similarly, cylindrical MPGD layers (micromegas or μRWELL detector) at the inner and the outer radius with the appropriate readout strip design can be added to a Straw tubes or Drift chamber tracker to provide the sub-millimeter position resolution in the direction along the beam axis.

#### 4.1.1.2 Vertex/Silicon Tracker

A silicon vertex and tracking detector at the EIC has to fulfil three tasks:

- Determine the vertex with the high precision (in conjunction with the forward-backwards silicon trackers).
- Allow the measurement of secondary vertices for heavy-flavor physics (e.g. $F_{2,\,charm}$).
- Low-$p_T$ tracking, extending the range of the central tracker to tracks that curl up too much to be detected in the main tracker.

To fulfil these tasks requires a small pixel size (20x20 μm$^2$), and low material budget. The most promising technology to satisfy these requirements are Monolithic Active Pixel Sensors (MAPS). Current, state-of-the-art MAPS are the MIMOSA sensor used for the STAR HFT at RHIC [9], and the ALPIDE sensor designed for the ALICE ITS upgrade [10]. Whilst the MIMOSA sensor is a traditional MAPS detector based on charge collection by diffusion, the ALPIDE sensor is the first of a new generation of MAPS fabricated in a commercial CMOS imaging technology on high resistivity epitaxial layer. This technology allows to deplete part of the sensor volume with a reverse bias voltage of -6 V. Charge is thus in part collected by drift. A cross section of an ALPIDE pixel illustrating the process is shown in Figure 15. A depletion region develops around a small collection electrode. Electronics is hosted in separated p-wells. This pixel layout configuration provides a small detector capacitance to ensure low noise, fast readout, and low power consumption. Moreover, the availability of multiple nested wells offered by CMOS technologies allows the use of full CMOS electronics, and thus the integration of more advanced readout architectures with respect to the traditional MAPS rolling shutter readout used by the MIMOSA sensor.

The ALPIDE chip, developed by a collaboration formed by CCNU (Wuhan, China), CERN, INFN (Italy), and Yonsei (South Korea), contains a novel low-power in-pixel discriminator circuit that drives an in-matrix asynchronous address encoder circuit, read out by an end-of-column lossless data compression. The digitization of the signal within the pixel eliminates the need for an analogue column driver, reduces the power consumption significantly and allows for fast read-out. The ALPIDE chip features a 4 μs integration time, a power consumption of less than 39 mW/cm$^2$, and an intrinsic spatial resolution of below 5 μm.

With the ALPIDE sensor and the final stave and FPCB design used in the ITS, a total layer thicknesses of ~0.3 $X/X_0$ can be reached for relatively short staves (up to 40cm or so, sufficient for a typical EIC detector barrel vertex tracker).

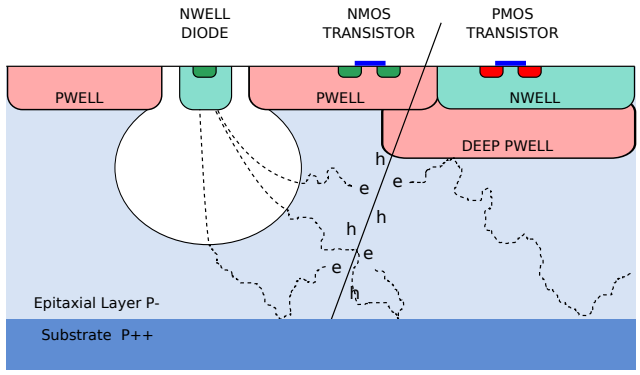


*Figure 15: Schematic cross section of an ALPIDE pixel in the TowerJazz 180 nm CMOS imaging technology with deep p-well allowing integration of full CMOS logic [10].*

With respect to ALPIDE, the EIC would certainly benefit in improvements in the integration time[2] as well as in a further reduction of the energy consumption and material budget going towards 0.1-0.2% radiation length per layer. Timing-wise the ultimate goal of this technology would be to time stamp the bunch crossings where the primary interaction occurred. This may impose different requirements depending on the machine design, but is in general driven by the expected interaction rate at the highest luminosities.

More recent developments of MAPS sensors have focused on achieving full depletion of the sensor volume in order to collect charge by drift. Charge collection through drift results in faster signals, less charge spreading at the collection electrode leading to better signal-to-noise, and improved radiation hardness with respect to collection by diffusion. Whilst radiation hardness and fast charge collection are significant for experiments at the HL-LHC, the capability of collecting larger charge in smaller pixels would be beneficial to improve spatial resolution in high precision lepton-hadron and lepton-ion colliders.

A number of commercial CMOS technologies providing either high-voltage (HV) capabilities and/or high resistivity substrates (HR) have been investigated to develop depleted MAPS (DMAPS) sensors. The more mature developments are in the TowerJazz, LFoundry, and AMS processes [11]. Two-pixel layout configurations are investigated depending on the technology: one with small collection electrode and separated electronics, such as ALPIDE, and one with a large collection electrode containing the electronics. Figure 16 shows a cross section of the two layouts. The former has been developed using a modified version of the TJ 180 nm CMOS imaging process used for ALPIDE, where a deep planar junction in the epitaxial layer allows for the depletion region to grow below the electronics [12]. A large collection electrode configuration is used in LFoundry and AMS to achieve full deple-

[2] A luminosity of $10^{34}$ cm$^{-2}$ s$^{-1}$ will bring the interaction rate to 500kHz or 1/(2 μs).

tion of the sensor volume with uniform electric field. Whilst the small collection electrode design offers the advantage of small sensor capacitance, the design with a large collection electrode can potentially provide higher radiation hardness.

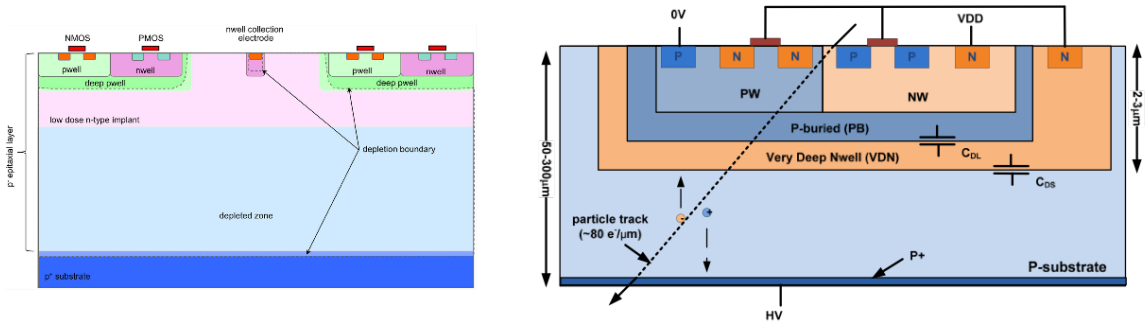


*Figure 16: Cross sections (not to scale) of a DMAPS detector where the electronics is placed outside (left, [12]) and inside (right, [13]) the collection electrode.*

Table 3 summarizes the main features of state-of-the-art DMAPS prototypes in commercial HV/HR-CMOS technologies. These prototypes have been developed for application at the HL-LHC in the ATLAS experiment. They have been optimized to cope with high particle rates and radiation levels and achieve a time resolution in the order of few tens of ns, in the right ballpark for the envisaged time stamping capability at an EIC vertex and tracking detector. For a given analogue performance, configurations with small collection electrode, having a small detector capacitance, enable the power consumption to be minimized and to design more compact front-end electronics, thus allowing a small pixel size. Different readout architectures have been developed to cope with the high particle rates [11]. Both synchronous and asynchronous readout architectures have been implemented. The synchronous readout architecture is based on a well-known concept used in the FE-I3 readout chip for the present ATLAS pixel detector, so-called column drain architecture [14]. Novel asynchronous readout concepts have been developed with the potential of matching the timing and rate requirements with a lower digital power consumption. Whilst the choice of collection electrode configuration is driven by the chosen CMOS technology, the choice of the readout architecture is independent of the CMOS technology in which the DMAPS sensor is implemented.

| | **ALPIDE** | **MALTA** | **TJ-MONOPIX** | **LF_MONOPIX** | **ATLASpix_Simple** |
|---|---|---|---|---|---|
| Experiment | ALICE ITS | ATLAS ITk pixel Phase II (outermost layers only) | | | |
| Technology | TJ 180 nm | Modified TJ 180 nm | | LF 150 nm | AMS 180 nm |
| Substrate resistivity [kOhm cm] | > 1 (epi-layer 18-25 um) | | | > 2 | 0.08 - 1 |
| Collection electrode | small | small | small | large | large |
| Detector capacitance [fF] | <5 | | | Up to 400 | |
| Chip size [cm x cm] | 1.5 x 3 | 2 x 2 | 1 x 2 | 1 x 1 | 0.325 x 1.6 |
| Pixel size [um x um] | 28 x 28 | 36.4 x 36.4 | 36 x 40 | 50 x 250 | 40 x 130 |
| Time resolution [ns] | 20 x $10^3$ | 25 | | | |
| Particle rate [kHz/mm$^2$] | 10 | $10^3$ | | | |
| Readout architecture | Asynchronous | | Synchronous, column drain | | |
| Analogue power [mW/cm$^2$] | 5.4 | < 120 | ~ 110 | ~ 300 | N/A |
| Digital power [mW/cm$^2$] | 31.5/14.8 | N/A | N/A | N/A | N/A |
| Total power [mW/cm$^2$] | 36.9/20.2 | N/A | N/A | N/A | N/A |
| NIEL [1MeV $n_{eq}$/cm$^2$] | 1.7 x $10^{13}$ | 1.0 x $10^{15}$ | | | |
| TID [Mrad] | 2.7 | 50 | | | |

*Table 3: Comparison of state-of-the-art MAPS (ALPIDE) and DMAPS sensors (MALTA [15,16], TJ-MONOPIX [17], LF_MONOPIX [17], ATLASPix [18]), designed respectively for heavy ion and proton-proton experiments at LHC. The power figures of the ALPIDE sensor refer to the inner/outer layers of the ALICE ITS [10]. Due to their recent developments, some power figures of the DMAPS sensors are not yet published.*

It is worth mentioning at this point, that more technologies have been investigated for DMAPS development (XFAB, ESPROS, Toshiba, Global Foundries, ST microelectronics, etc.). These have however at the time of writing not reached a fully monolithic design and exist only at the level of test structures with partial readout capabilities. They are thus not considered in the table.

Current DMAPS prototypes prove that this detector concept could bring the envisaged improvements for an EIC vertex and tracking detector with respect to the current baseline, i.e. the ALPIDE, with a dedicated R&D for this particular application. Building upon current developments, a DMAPS sensor for the EIC would benefit from having a small collection electrode, full depletion, and optimized low power analogue FE and readout architecture. Different design optimizations might be needed for the inner radii, which require very small pixel size and very low material, and for the larger radii, where time stamping capability could be added at the expense of slightly larger pixels and increased material. Simulations should inform the requirements in terms of pixel size and material at different radii to understand where time stamping capability could be added, without degrading impact parameter and momentum resolution.

DMAPS sensors, with the appropriate optimization, could be used as well in the forward and backward silicon trackers, as well as in the main tracker in case of an all-silicon solution.

In addition to the sensor technologies discussed here, development of lightweight services and support structures should attract attention in the EIC detector R&D community, to achieve a low material silicon vertex and tracking detector.

### 4.1.2 Forwards and Backwards Tracking

Tracking detectors in the endcaps in general serve the purpose to complement the central tracker at the larger $|\eta|$ where it typically does not provide sufficient number of hits, except probably for the all-silicon configuration. These detectors should cover moderately large surface areas behind the TPC endcap. Exceptionally high spatial resolution is not really required, although in order to help recover reasonably high momentum resolution at $p\approx$30-50 GeV/$c$ in the hadron-going direction the 50 μm spatial resolution per station is desirable.

It is also believed that in order to facilitate the reliable hadron PID in the forward gaseous RICH, a second set of large planar tracking detectors between the RICH volume and the electromagnetic calorimeter is desirable. Spatial resolution is not a concern here, but the

detectors should cover the surface area of several square meters. It is assumed that large area MPGDs (GEMs, Micromegas, μRWELL) can be used for these purposes.

The obvious complication with the (very) forward and the (very) backward trackers is vanishing bending power of the solenoid magnet for the shallow scattering angles. As an example, at a pseudo-rapidity $\eta$ = 3, which corresponds to roughly 100 mrad scattering angle, solenoid provides only 10% of its nominal maximum B·d$\ell$ integral in the bending plane. Therefore, one has to resort to using very thin detectors (in order to minimize the constant term in the momentum resolution expression) with very small pixel size (in order to minimize the slope in this same expression with the higher momenta).

MAPS technology is a natural choice, with all the benefits and all its drawbacks considered in detail in the previous section. It can be shown by direct Monte-Carlo modelling that 7-8 MAPS disks with 20 μm pixel size and 0.3% radiation length per layer installed between the nominal IP and roughly the TPC endcap location (1.0-1.2 m away from the IP) can provide the required momentum resolution in the whole pseudo-rapidity range and particle momentum range of interest for physics.

The alternative solution is a set of high-resolution GEM tracker stations installed up to the distances of ~3.0 m away from the IP. Monte-Carlo simulations show that this configuration should also work but would definitely require 50 μm or better spatial resolution per station.

Even if the MAPS disks are used for tracking at the very forward and very backward $\eta$, one may want to complement them with the fast low-material budget trackers like Cr-GEM, the GEM detector variety with the copper layer removed from the foils.

### 4.1.3 Roman Pots

One of the flagship measurements for an EIC is the measurement of the cross-section for Deeply Virtual Compton Scattering (DVCS) through the reaction channel $ep \rightarrow e'p'\gamma$. This is an important process because it gives access to the GPDs of gluons, allowing us to learn about their transverse spatial distribution inside the proton. One characteristic of these reactions is that the proton scatters at a very small angle and near beam energy. This makes it challenging to detect these protons, as it is necessary to verify that the proton remains intact and to ensure exclusivity of the measurement.

The expected distributions of the protons as a function of their polar scattering angle and momentum are shown in Figure 13 for collisions at different proton beam energies. Specialized instrumentation is needed to measure the protons that scatter at such small angles. Various experiments at other facilities have implemented forward proton taggers as Roman Pots to access these protons. The Roman Pots need to be designed such that they can be retracted away from the beam during injection, and moved towards the beam once stable conditions are achieved. This allows the detectors to be placed as close to the beam

as possible, maximizing the acceptance to these protons.

The distance to the core of the beam to which the Roman Pots can be placed depends on the beam width at the location of the station. Previous experience is that the safe operating distance is roughly 10σ of the beam width from the core of the beam. The Roman Pot location has to be carefully coordinated with the machine and magnet design group to ensure there is sufficient acceptance through the magnets, as well as sufficient dispersion to pull off-momentum protons out of the beam into the detectors and a small enough beam size at the location of the Roman Pots so that they can be placed as close as possible to the beam. Additional R&D efforts on sensor design are ongoing in regards to the development of "edgeless" sensors or sensors that can be tailored to the shape of the beam to further increase the acceptance to these small angle scattered protons.

Simulations have been performed to investigate the momentum range needed for a measurement of the DVCS process. This is summarized in Figure 17 below, which shows the expected uncertainty on the gluon impact parameter extracted from the measurement using 10 $fb^{-1}$ of data and full acceptance over the $|t|$ range indicated in the figure. Figure 17 shows the ideal case listed in the requirements. *Figure 18* and Figure 19 demonstrate the negative effect of the acceptance truncation at either the lower or higher end of the stated $|t|$ range, respectively.

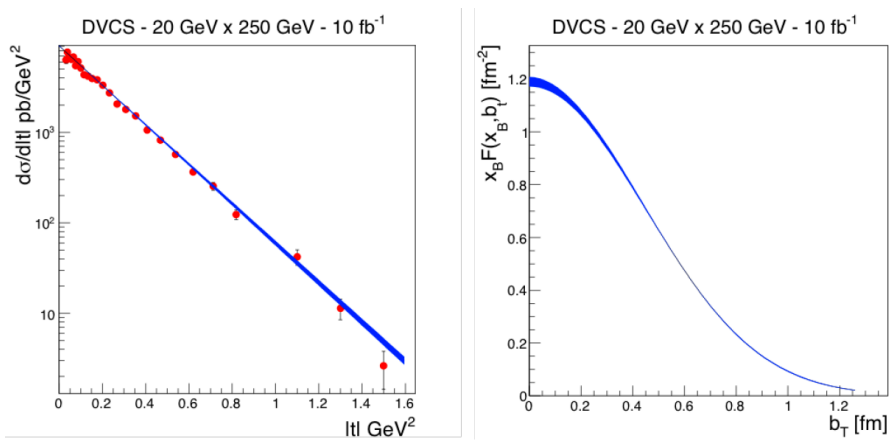


*Figure 17: (Left) A simulation of the measurement of DVCS cross section for 20x250 GeV ep-collisions representing statistics from 10 $fb^{-1}$ of data. The measurement also assumes an acceptance range of $0.18 < p_T < 1.3$ GeV/c. The band represents the fit to the simulated data, along with its associated uncertainties. (Right) The translation of the cross-section measurement to the measurement of the structure function $F_2$ with its associated uncertainties.*

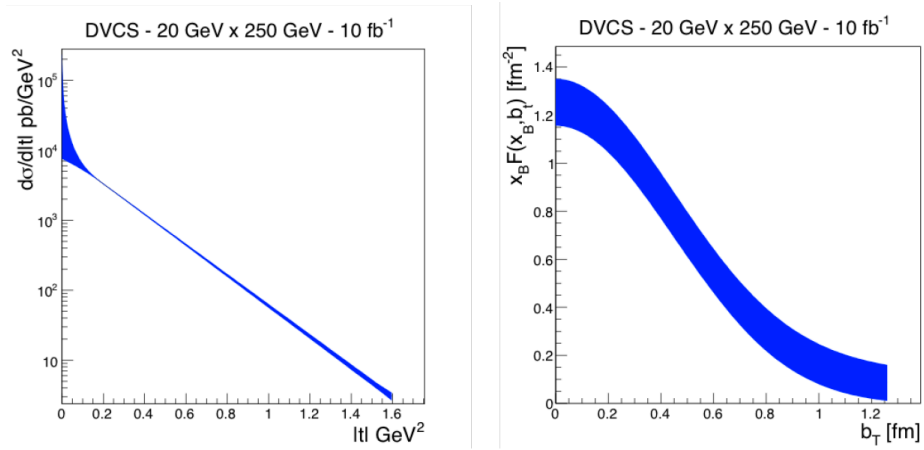


*Figure 18: Same as* Figure 17*, but for an acceptance range of 0.44 < $p_T$ < 1.3 GeV/c*

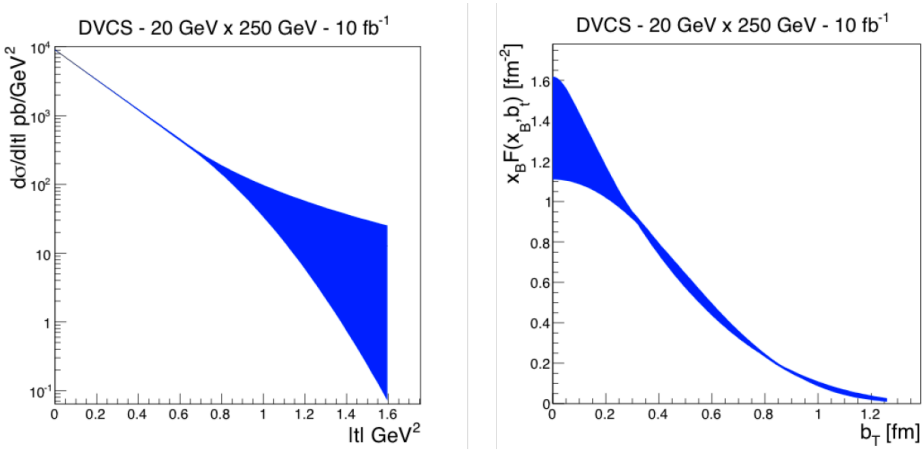


*Figure 19: Same as Figure 17 but for an acceptance range of 0.18 < $p_T$ < 0.8 GeV/c*

Basic requirements on the Roman Pot systems based on simulations and knowledge from other facilities are summarized below:

1) Installed in a warm region of the IR.
2) ZDC detectors required to veto the nuclear breakup.
3) Proton acceptance in the range of 0.18 < $p_T$ < 1.3 GeV/$c$ (0.03 < |t| < 1.7 GeV$^2$).
4) Multiple stations may be required to allow for efficient tracking, as well as greater acceptance over a wider range in |t|.
5) A momentum resolution comparable to that of currently achieved at STAR.

### 4.1.4 Low-$Q^2$ Tagger

Access to a wide range of the relevant kinematic variables are paramount to allow for a flexible physics program at the EIC. The focus of this section is on the available $Q^2$ coverage at smaller values. The $Q^2$ of an event can generally be reconstructed by measuring the angle and energy of the scattered electron in a DIS event (though there are other methods available that rely on the reconstruction of the hadronic final state). *Figure 20* as well as *Figure 21* show the distribution of the scattering angle of the electron and its momentum as it correlates to the $Q^2$ of the event as simulated with PYTHIA for 20 GeV electrons colliding with 200 GeV protons. The distributions look similar for other collision energies. A strong correlation is observed. Most of the events at low $Q^2$ ($Q^2 < 0.1$ GeV$^2$) result in the electron scattering at very small angle (less than $2^0$ from the electron beam direction) with a momentum very close to the beam momentum. This implies that electrons from these events will be outside of the main detector acceptance and thus a dedicated device to measure them is required.

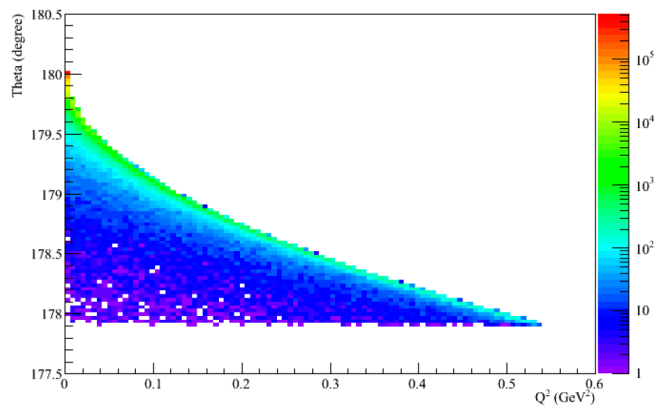


*Figure 20: A PYTHIA simulation of 20 GeV electrons colliding with 250 GeV protons displaying the correlation of the scattered electron angle with $Q^2$.*

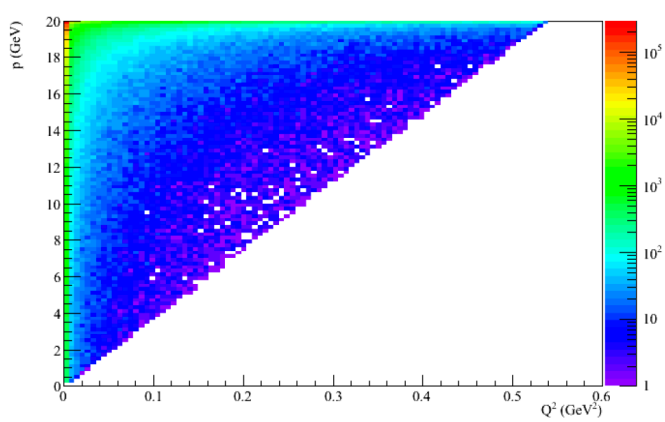


*Figure 21: A PYTHIA simulation of 20 GeV electrons colliding with 250 GeV protons displaying the correlation of the scattered electron momentum with $Q^2$.*

Such a device needs to be incorporated into the machine IR design to ensure that these electrons are sufficiently pulled away from the beam to detect them. The detector needs to have good energy and position resolution as well in order to calculate the scattering angle of the electron and thus reconstruct the $Q^2$ of the event. Additionally, it would be helpful to have a combination of tracking and electromagnetic calorimetry, which would assist in vetoing photons hitting the detector and help with electron identification.

## 4.2 Calorimetry

Calorimeters measure particle energy by total absorption. Electromagnetic ones measure the energy of electrons and photons as they interact with matter producing electromagnetic showers. Hadronic calorimeters measure response to the hadronic showers, which contain both an electromagnetic and a strong interaction component, e.g. fission, knock-off, delayed photons.

### 4.2.1 Electromagnetic Calorimeters

A typical high-performance ElectroMagnetic (EM) calorimeter is a 2D matrix of light-transparent, homogeneous, crystal blocks with dimensions large enough to contain the complete shower of secondary particles. Crystal calorimeters have been used in nuclear and high energy physics for their high resolution and detection efficiency. The readout of crystal calorimeters is light-based, and the classical option is photomultiplier tubes. Advanced readout configurations include Avalanche Photo-Diodes and Silicon Photomultipliers. Homogeneous electromagnetic calorimeters have been used at, e.g. JLab ($PbWO_4$), KTeV (CsI), BaBar and Belle (CsI(TI)), CMS ($PbWO_4$) and L3 (BGO) experiments. The latter two are complemented by hadronic calorimeters. Table 4 lists some of the properties of these and few other systems.

Most calorimeters in high energy physics are sampling as the cost of homogenous crystal ones would be unaffordable. Sampling calorimeters consist of an active (readout, e.g. scintillator or Cherenkov radiator) and a passive (absorber, e.g. Pb, Cu, W) component. They provide high granularity in both lateral and longitudinal direction, but energy resolution is substantially lower than that of crystal calorimeters. The key parameter for this type of calorimeter is the sampling fraction, which is the ratio of energy deposited in active and passive layers. There are many ways to build sampling calorimeters ("sandwich", "spaghetti", etc), where the sandwich type has been most popular. Light collection efficiency is an important consideration for sampling calorimeters as sampling fluctuations directly impact energy resolution. The most popular solutions are SPACAL (Pb, scintillating fibers) and sandwich with Wave-Length-Shifting (WLS) fibers crossing through ("Shashlik"). In both cases the fibers are bundled to the PMT. Examples of sampling calorimeters are provided in Table 4.

| Technology | Experiment | Depth | Energy resolution | Readout |
|---|---|---|---|---|

| | | | | |
|---|---|---|---|---|
| NaI(Tl) | Crystal Ball | $20X_0$ | $2.7\%/E^{1/4}$ | |
| $Bi_4Ge_3O_{12}$ (BGO) | L3 | $22X_0$ | $2\%/\sqrt{E} + 0.7\%$ | |
| CsI | KTeV | $27X_0$ | $2\%/\sqrt{E} + 0.45\%$ | |
| CsI(Tl) | BaBar | $16\text{-}18X_0$ | $2.3\%/E^{1/4} + 1.4\%$ | SiPM |
| CsI(Tl) | Belle | $16X_0$ | $2\%/\sqrt{E}$ | SiPM |
| $PbWO_4$ | CMS | $25X_0$ | $3\%/\sqrt{E} + 0.5\% + 0.2/E$ | APD |
| $PbWO_4$ | Primex | | $1.75\%/\sqrt{E} + 1.15\%$ | PMT |
| $PbWO_4$ | PANDA | | $<2\%/\sqrt{E} + <1\%$ (req.) | LAAPD |
| $PbWO_4$ | NPS | | $<2\%/\sqrt{E} + <1\%$ (req.) | PMT |
| Lead glass | OPAL | $20.5X_0$ | $5\%/\sqrt{E}$ | |
| Liquid Kr | NA48 | $27X_0$ | $3.2\%/\sqrt{E} + 0.42\% + 0.09/E$ | |

*Table 4: Examples of homogeneous EM calorimeter systems based on crystals [19, 20, 21, 22, 23, 24, 25, PANDA,NPS], lead glass [26] or noble gas liquids [27,28].*

| **Technology** | **Exp.** | **Depth** | **EM Energy resolution** | **Readout** |
|---|---|---|---|---|
| Scintillator/depleted U | ZEUS | $20\text{-}30X_0$ | $18\%/\sqrt{E}$ | PMT |
| Scintillator/Pb | CDF | $18X_0$ | $13.5\%/\sqrt{E} + 2.5\%$ | |
| Scintillator fiber/Pb spaghetti | KLOE | $15X_0$ | $5.7\%/\sqrt{E} + 0.6\%$ | PMT |
| Liquid Ar/Pb | NA31 | $27X_0$ | $7.5\%/\sqrt{E} + 0.5\% + 0.1/E$ | |
| Liquid Ar/Pb | SLD | $21X_0$ | $8\%/\sqrt{E}$ | |
| Liquid Ar/Pb | H1 | $20\text{-}30X_0$ | $12\%/\sqrt{E} + 1\%$ | |
| Liquid Ar/depl. U | D0 | $20.5X_0$ | $16\%/\sqrt{E} + 0.3\% + 0.3/E$ | |
| Liquid Ar/Pb accordion | ATLAS | $25X_0$ | $10\%/\sqrt{E} + 0.4\% + 0.3/E$ | |
| Scintillator/Pb | CLAS | $15X_0$ | $10\%/\sqrt{E}$ | PMT |
| Scintillator/Pb | GluEx | $15X_0$ | | SiPM |

*Table 5: Examples of sampling EM calorimeter systems based on layers of low $X_0$ passive material interleaved with active material based on plastic scintillators [29, 30, 31, 32], gas [33, 34], silicon + dense materials (Fe, Pb, W, ...). The energy resolution depends on sampling fluctuations.*

The regions and functions of the EM calorimeters envisioned for the EIC are:

1. ***Lepton/Backward direction:*** detect the scattered lepton with high energy resolution. At rapidities $\eta \lesssim -2$ the electron energy measurement comes mainly

from the calorimeter. The segmentation has to be good enough for particle identification, *e.g.* to separate electron and photon from DVCS events.

2. ***Ion/Forward direction:*** detect high-x SIDIS particles and the electromagnetic part of high-x jets with high resolution.
3. ***Barrel/Mid rapidity:*** provide particle identification for leptons in a region where the hadron background is large. These include photons from DVCS, vector mesons, $\pi^0$ and electromagnetic part of jets.

#### 4.2.1.1 Barrel Calorimeter

The choice of calorimetry at central rapidity is driven by the need to provide electron identification in a region where the hadron background is large. Measuring the ratio of the energy and momentum of the scattered lepton, typically gives a reduction factor of ~100 for hadrons. In this region the energy (momentum) measurement is provided by tracking detectors, and thus noticeably worse energy resolution of the calorimeter suffices.

Depending on the center-of-mass energy the rapidity distributions for hadrons (both charged and neutral) and the scattered lepton do overlap and thus need to be disentangled (see Fig. 10). The kinematic region in rapidity over which hadrons and photons need to be suppressed with respect to electrons depends on the center-of-mass energy. For lower center-of-mass energies, electron, photon and charged hadron rates are roughly comparable at 1 GeV/$c$ total momentum and $\eta$ = -3. For the higher center-of-mass energy, electron rates are a factor of 10-100 smaller than photon and charged hadron rates, and comparable again at a 10 GeV/$c$ total momentum. The kinematic region in rapidity over which hadrons and also photons need to be suppressed, typically by a factor of 10 - 100, shifts to more negative rapidity with increasing center-of-mass energy.

To satisfy the Particle Identification requirements in the barrel, EM calorimetry should provide:

1. ***Compact design*** as space is limited
2. ***Energy resolution*** < (10-12%/$\sqrt{E}$)

There is no need in 2D projectivity. It is anticipated that a sampling calorimeter design with relatively modest specifications would meet the requirements.

#### 4.2.1.2 Forwards and Backwards Calorimeter

The choice of calorimetry at backward rapidity $-4 < \eta < -1$ is driven by the requirement to detect the scattered lepton with high energy resolution, which for rapidities $|\eta| > 3.5$ is determined by the EM calorimeter alone. Furthermore, the granularity of the calorimeter has to be good enough for particle identification, e.g. to separate electron and photon from DVCS. Calorimetry at forward rapidity $1 < \eta < 3.5$ is driven by the need to identify hadrons produced in semi-inclusive processes, in particular at large $x$.

Figure 9 showed the momentum vs. rapidity distributions in the laboratory frame for photons originating from deeply virtual Compton scattering (DVCS) for different lepton and proton beam energy combinations. For lower lepton energies, photons are scattered in the forward (ion) direction. With increasing lepton energy, photons increasingly populate the central region of the detector. At the highest lepton beam energies, photons are even produced backward (in the lepton-going direction), very close to the electron cluster. Overall, as already stated earlier, a EM calorimetry rapidity coverage of -4 < $\eta$ < 1 is needed for DVCS photons.

Figure 22 shows the impact of high-resolution crystal calorimetry on ($x$, $Q^2$) determination at small scattering angles, where the tracking resolution is poor. The quality of the physics measurement is determined to a large extent by the level of bin-to-bin migration in the 2D ($x$, $Q^2$) kinematic plane. The past experience, in particular the HERMES Collaboration data analysis, indicates that acceptable "bin survival" level (the probability to register the event in the same kinematic bin where it originally occurred), which effectively determines the kinematic reach, should be of on the order of at least 0.6-0.7, spanning from the maximum values of $y$ down to the region of $y \sim 0.01$ (where $y$ is the DIS variable, describing a fraction of the beam electron energy carried by the virtual photon). A significant fraction of the "small $y$" kinematic domain is characterized by small electron scattering angles and large energy. As discussed above, tracker momentum resolution, which is typically used for the scattered electron track parameter determination, degrades rapidly under these circumstances because of the vanishing effective B*dl integral of the central part of the solenoid field. A crystal calorimeter with the sufficiently high energy resolution in the electron-going direction end-cap can potentially circumvent this problem. Namely the scattered electron momentum can be taken as a weighted mean of the momentum measured by the tracker system and the energy measured by such a calorimeter. A high resolution crystal calorimeter for $\eta$ < -2 (PWO crystals) improves the available $y$ range considerably. At rapidity -2 < $\eta$ < 1 the resolutions requirement can be relaxed. The optimal solution would thus be a combination of an inner (PWO crystal) and outer (sampling) calorimeter.

Overall, the ***inner*** EM endcap calorimeter for rapidity $\eta$ < -2 should provide:

1. Good ***resolution in angle*** to at least 1 degree to distinguish between clusters,
2. ***Energy resolution*** < (1.0-1.5 %/$\sqrt{E}$+0.5%) for measurements of the cluster energy,
3. ***Time resolution*** to < 2ns
4. Cluster threshold: 10 MeV
5. Ability to withstand radiation down to at least 1 degree with respect to the beam line.

The ***outer*** EM endcap calorimeter for rapidity -2 < $\eta$ should provide:

1. ***Energy resolution*** < 7%/$\sqrt{E}$ for measurements of the cluster energy,
2. ***Compact readout*** without degrading energy resolution
3. ***Readout segmentation*** depending on the angle

Modelling also shows that in order to make a clear positive impact on the scattered electron kinematics determination, a crystal calorimeter ($PbWO_4$) in the inner part of the electron-going end-cap should have a constant term of at most ~0.5%, while a stochastic term on the order of 1.0-1.5% would suffice.

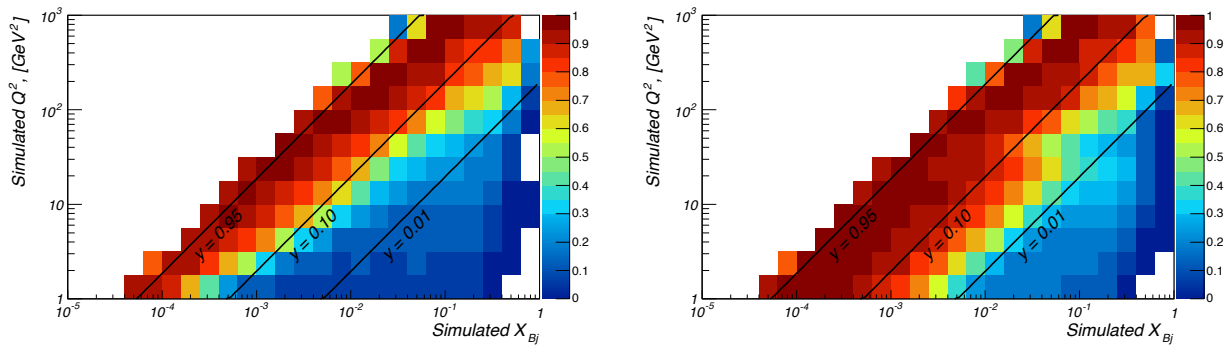


*Figure 22: Inclusive DIS event migration in the {x, $Q^2$} kinematic plane. Pythia 20x250 GeV events, external bremsstrahlung turned off. Only the area with survival probability > 0.6-0.7 is suitable for the conclusive analysis. Left panel: only the tracker information is used to calculate scattered electron momentum. Right panel: same events, but a weighted mean of the tracker momentum and the crystal calorimeter energy is used. Calorimeter resolution is taken to be $\sigma_E/E$ ~ 2.0%/$\sqrt{E}$ for pseudo-rapidities below -2.0 and ~ 7.0%/$\sqrt{E}$ for the rest of the acceptance.*

### 4.2.2 Hadron Calorimeters

The requirements on hadron calorimetry are imposed by the jet energy resolution and linearity of response in the hadron-going direction. For the LHC physics program the jet energy resolution requirements is ~3%. Hadronic calorimetry at EIC in the forward region, 1< $\eta$ < 4 with a stochastic term of the hadronic energy resolution of seems to be sufficient for accessing gluon polarization using di-jets to tag photon-gluon fusion events. These studies require the highest energies ($\sqrt{s}$=141 GeV) and luminosity to accumulate statistics at high $p_T$. The dominant contribution to jet energy resolution at these high energies comes from the constant term, which includes nonlinearities. For studies at low $p_T$ requiring sufficient resolution at large x for accessing inclusive jet cross-sections in DIS, the stochastic term becomes important. For optimal resolution for jet identification, a hadronic energy resolution of better than that achieved at ZEUS (35%/$\sqrt{E}$) combined with low EM energy resolution would be preferable. At HERA, uncertainties at low and medium values of $Q^2$ were dominated by the jet energy scale uncertainties, which were on the order of 1-2% and translated into 5-10% uncertainties in the cross section.

### 4.2.3 Zero Degree Calorimeter

For many different processes, collision geometries in *e*A-scattering can be determined by utilizing the Zero-Degree Calorimeter (ZDC). The number of forward neutrons produced and detected in the ZDC is expected to be sensitive to the path length of the parton and fragmentation of the colliding nucleon along the virtual photon direction in the nucleus. The maximum path corresponds to the impact parameter $b \sim 0$. Therefore the most "central" collisions in *e*A can be identified from the events with the highest neutron multiplicity. Selecting events with centrality > 5% will enhance the effective A in the reaction, which is crucial for any measurements of non-linear effects in QCD. This selection will effectively maximize nuclear effects in SIDIS *e*A collisions such as for the di-hadron correlation studies. This fact and the requirement that the four-momentum transfer $t$ in diffractive reactions with a charge exchange is obtained from the neutron, requires a ZDC with much higher energy and position resolution than is currently achieved at RHIC. Qualitative estimates of the ZDC specifications require further modelling effort.

## 4.3 Particle ID

Excellent particle identification (PID) is an essential requirement for a future EIC detector. In particular, quark flavor separation is much more important for the EIC than for most high-energy physics (HEP) experiments. The impact of this is twofold. First, the PID systems have a much larger impact on the overall configuration of the detector; and second, the synergies with HEP R&D are more limited than in the case of, for instance, tracking and calorimetry.

Another aspect particular to the EIC, is that the distribution of final-state particles is very asymmetric (due to the large difference in energies of the incoming lepton and ion beams), and that the physics of interest requires detection and identification of particles over the full angular range. Providing this coverage despite the asymmetric collisions requires an integrated suite of detector subsystems.

### 4.3.1 Hadron PID

For hadron identification, the only type of detector capable of providing the required momentum coverage (5-50 GeV/$c$, depending on polar angle) is based on Cherenkov radiation – although the same principle can have different implementations, designed to address the wide range of requirements in the different parts of the detectors – both in terms of particle momentum and available space. The lowest momenta (up to a few GeV/$c$), can be covered by measurement of the time-of-flight (TOF) or $dE/dx$ in gaseous central trackers (like a TPC) along the charged particle trajectory.

Simulations show that in order to satisfy the physics goals of the EIC, it is desirable to provide π/K identification in the central barrel up to 5-7 GeV/$c$, in the electron-going endcap up ~10 GeV/$c$, and in the hadron-going endcap one would need to reach ~50 GeV/$c$. To

address the overall hadron identification requirements, an integrated solution is required, employing different technologies in different parts of the detector.

In the hadron endcap, the only possibility of reaching the maximum required momentum is to use a Ring-Imaging Cherenkov (RICH) detector with a light gas ($CF_4$ or $C_2F_6$) as radiator. However, in order to provide continuous PID coverage, this needs to be complemented by a radiator with a higher index of refraction (such as aerogel). The two radiators can be part of one system (a dual-radiator RICH), sharing the same optics and readout, or be implemented as two separate systems. A third system (TOF or $dE/dx$) is needed to cover the lowest momentum range, below the pion threshold of the aerogel RICH. The best combination of the refractive index of the gas and aerogel radiators, the momentum reach of the third system, and the corresponding optics and electronics are being investigated as part of the ongoing EIC detector R&D. The ideal configuration will depend both on the technical details of the PID subsystem(s), but also on the overall design of the detector (space, magnetic field, *etc*).

In the central barrel, the main challenge is to have a compact detector that can cover a large area at reasonable cost while providing the desired momentum reach. A detector that currently can address all three of these requirements is the one based on Detection of Internally Reflected Cherenkov light (DIRC). Other RICH detectors are less compact and would be too costly due to the large sensor area that would be needed, while the flight path is too short to obtain the desired performance even with the very high-resolution TOF systems (yet with 5 ps resolution and a 1 m flight path, TOF could provide reasonable $\pi/K$ separation up to about 5 GeV/$c$).

In the electron-going endcap, space is constrained by the desire to make the most effective use of the EM calorimeter, which (at least in the inner part) needs to include high-resolution crystals (*e.g.*, $PWO_4$). Thus, the balance of the three criteria (size, cost, and performance) is shifted towards performance, and a compact aerogel detector becomes the best choice. A more compact option with lower performance, such as disc DIRC, would be technically feasible, but in this part of the detector space is not as restricted as in the barrel.

### 4.3.2 Electron identification

For an Electron-Ion Collider, it is also crucial to identify the scattered electron amid a background of negatively charged pions. Electron identification is also important for production of particles (*e.g.*, charmonia), which decay into leptons. Here, the main detector system is the electromagnetic (EM) calorimeter, which provides e/π separation over the full momentum range. The PID systems primarily intended for hadron identification can also provide an important supplementary capability for e/π. This is particularly important at low momenta (below 2-3 GeV/$c$), where a large pion background is expected, and the suppression provided by the EM calorimeter (~ 100:1) is not sufficient. By combining the

EM calorimeter with a Cherenkov detector, this suppression factor can be increased, effectively extending the kinematic reach.

It would also be possible to add an e/π capability to the central tracker, for instance in the form of a hadron-blind detection (HBD) functionality coupled to a TPC (radial HBD readout in the case of a typical TPC with longitudinal drift, or an endcap HBD readout in an rTPC configuration with the radial drift). Such an HBD would cover the momentum range of relevance for identification of the scattered electron, but a dedicated rTPC for the electron-going endcap would require a significant amount of space that could be used for other tracking technologies. From this point of view, extending the e/π momentum reach of the (aerogel) Cherenkov instead of adding another system would be a more universal approach.

In the hadron-going endcap, in addition to electromagnetic and hadronic calorimetry, a large gas Cherenkov detector can also provide $e/\pi$ separation up to 10-15 GeV/$c$. In order to add supplementary electron identification at high momenta, one could introduce a transition-radiation detector (TRD), which can perform electron identification in the 2-100 GeV/$c$ range. An additional benefit of a TRD is that it also provides tracking information in the area between RICH and the electromagnetic calorimeter, helping to improve momentum and position resolution.

### 4.3.3 Detector technologies

In the following, various detector technologies considered for particle identification are described in somewhat more detail.

#### 4.3.3.1 Gas- and dual-radiator RICH

The large gas RICH in the hadron-going endcap is one of the most important systems of the EIC detector, but perhaps also the one offering most choices. The most fundamental question is whether to build gas and aerogel RICH detectors separately or use a dual-radiator RICH. However, within each of the two categories there exists a yet another set of choices.
The dual-radiator RICH is restricted to having mirrors that reflect the Cherenkov light outward (away from the beam line). This is necessary, since the near-beam area on the hadron side has the highest radiation levels in the entire detector. This not only creates a lot of background hits, but the dose is too high for the currently available photosensors. The additional benefit of this configuration is that Cherenkov light produced in the gas does not have to pass through the aerogel.

To enhance the signal, one could filter out the shortest wavelengths from the aerogel so that the collected UV light would only come from the gas. These short wave length photons undergo Rayleigh scattering as they pass through the aerogel, losing the Cherenkov angle information, and would only contribute to the noise if allowed to reach the focal plane. The simplest optics would consist of spherical mirrors arranged in sectors with 3D focusing, ensuring that the total photosensor area is small, as this is the main cost driver for this

type of detector. While simple spherical mirrors do not produce a flat focal plane, which can introduce aberrations, the EIC R&D suggests that this issue can be addressed in a relatively straightforward way by adjusting the geometrical layout of the photosensors.

An advantage of the dual-radiator RICH is that it is easy to ensure full coverage both in angle and momentum – the latter by matching the refractive indices of the gas and aerogel (n=1.02 aerogel and $C_2F_6$ gas seems to be a very promising combination).

A gas-only RICH can in principle be built to the same geometry as a dual-radiator RICH. One of the reasons for choosing a gas-only RICH is to have inward reflecting mirrors (i.e., towards the beam). This choice changes the overall shape of the RICH detector from a cylinder ("pillbox") to a cone (without its top, and with a rounded bottom). Depending on the overall layout of the detector, this may be easier to integrate with the other subsystems. The radiation issue associated with a focal plane close to the beam line is addressed by using GEM-based readout, which is more radiation hard than optical photosensors such as MCP-PMTs or SiPMs. CsI used as a photocathode material in the GEM-based scheme is sensitive only in the UV, making it a reasonable match for $CF_4$ radiator, which is the lightest of the gases typically used for Cherenkov detectors. However, since the refractive index of the gas changes rapidly at short wavelengths, and we cannot measure the "color" of the photon, chromatic effects become a substantial source of uncertainty. In the scope of EIC Detector R&D program it was demonstrated however that a relatively short (1m) RICH detector of this type should in principle be able to provide $\pi/K$ separation better than $3\sigma$ up to the momenta 40-50 GeV/$c$.

An initial comparison carried out between the gas-only and dual-radiator RICH options indicated a comparable momentum reach using $CF_4$ gas in the former and $C_2F_6$ in the latter – both fulfilling the EIC requirements. The main difference is on the other (low) side of the momentum range. When combined with an aerogel RICH, the lighter gas provides an overlap in coverage only in threshold mode for $\pi/K$ and not at all for K/p. If continuous coverage would be desired, it may be possible to find an alternative gas or gas mixture, with a higher index of refraction, but retaining properties like transparency in the UV.

#### 4.3.3.2 Compact Aerogel RICH

Proximity focusing aerogel RICH detectors provide reasonable performance in a small footprint. This can be improved even further by using two layers of aerogel with precisely matched indices of refraction to create a focusing effect at the high end of the covered momentum range. However, while such a detector could be used for the EIC, recent R&D suggests that cost, size, and momentum coverage could all be significantly improved by using lens focusing (a Fresnel lens would be preferable, but a spherical lens could be an alternative). The latter naturally leads to a modular design (hence mRICH), where each module has its own lens and readout. The main advantages of using a lens is that it creates a smaller, but sharper ring image, and that it centers the ring in the middle of the photosensor plane even if the hit was in a corner.

While the photosensors require a smaller pixel size (2-3 mm), the area can be reduced, leading to improved performance and reduced cost. In addition, a lens allows for more effective focusing, which makes it possible to shorten the module. The modular design makes the aerogel mRICH very flexible and easy to integrate with the EIC detector. It also allows for a projective arrangement, which can reduce the angular range of particle tracks impinging on the detector. This in turn further reduces the required sensor area. One thing to keep in mind is that while the EIC R&D currently focuses on one representative configuration to demonstrate the performance of the mRICH, it would be quite easy to use different variations in different parts of the EIC detector. For instance, while the prototype aims for 3σ π/K separation up to 8-9 GeV/$c$, increasing the focal length and reducing pixel size will make a module slightly longer but improve the performance. Longer modules can be used where space is available and performance is essential, while shorter modules can be used where integration with other systems imposes constraints on the overall geometry. In a similar way, different modules can use different photosensors. For instance, modules placed closer to the beam could use MCP-PMTs (which are more radiation hard), while modules further away could use SiPMs (which are not significantly affected by magnetic fields, regardless of orientation).

#### 4.3.3.3 Barrel DIRC Detector

This detector uses total internal reflection in a very precisely machined and polished bar with high refractive index (quartz), which also acts as a radiator, to collect the Cherenkov photons on a small sensor plane. While the quartz bars are expensive, they cost much less per unit area than the cheapest photosensors. In addition, the bars are very thin (2 cm) even with support structures included (5-6 cm), making the DIRC ideal for the large barrel region of the central detector, where radial space is at a premium. The key to the performance of DIRC detectors lies in the optics projecting the photons emerging from the bar onto a focal plane, and the possibility to measure the time of propagation for the photons. The original BaBar DIRC used simple pinhole focusing, and the timing resolution was only about 2 ns, which was only used to remove the out-of-time background hits. Relying on spatial imaging only ($x, y$ coordinates in the focal plane), it reached 3σ $\pi/K$ separation for momenta almost up to 4 GeV/$c$. Since then the development has taken three paths. One was the addition of focusing optics, as demonstrated by the FDIRC R&D at SLAC (which uses mirror-based optics). The second is exemplified by the Belle II TOP DIRC, which relies primarily on timing and only has a limited spatial imaging capability. While the performance of the TOP is comparable to that of the original BaBar DIRC, it achieves this with a very small image expansion volume and compact readout, which was the only way to make it fit the Belle II detector, which was not originally designed for a DIRC. Another advantage of the TOP scheme is that its wide radiator bars ("plates") are cheaper per unit area than those of the BaBar DIRC. The third path is to combine spatial imaging with a good timing (better than ~100 ps) to perform 3D ($x, y, t$) reconstruction. The joint PANDA and EIC R&D effort has shown that this approach is feasible and promises to deliver very high performance (4σ π/K separation at 6 GeV/$c$). The configuration explored for the EIC uses newly developed advanced lenses for focusing, for a sharper ring image and significantly

increased photon yield. The lens-based optics also allows one to use a compact expansion volume, which facilitates integration with other subsystems.

In addition to providing excellent PID, the High-Performance DIRC could also be used for precision event timing. The BaBar DIRC demonstrated that, by comparing the expected propagation times from all Cherenkov photons in an event to the measured times in an iterative process, the event time can be reconstructed with a precision limited primarily by the timing resolution of the sensors and electronics.

#### 4.3.3.4 Time-of-Flight (TOF)

The role of TOF measurements is to provide hadron identification at low momenta, where other subsystems (like aerogel-based RICH) run out of stem. Current examples of large TOF systems in use today typically achieve O(100 ps) resolution, but the R&D is ongoing to improve this significantly. Several groups have achieved ~5 ps TOF resolution using detectors based on MCP-PMT's. mRPCs have demonstrated ~20 ps timing. Development in TOF technology is also being driven by high energy physics, where timing of order 10-30 ps is required to deal with the increased event pileup after the high-luminosity upgrade of the LHC. As part of this R&D, LGAD (Low Gain Avalanche silicon Detectors) have now been demonstrated to be capable of <30 ps resolution. An EIC application could be to cover the smaller angles (close to the beam pipe) for a gas-only RICH where there is no space to place mRICH modules. This is also the location with the longest flight path, which is as important as timing resolution for achieving a certain level of TOF PID performance. At the typical distances of 4 m available on the hadron-going side, a 10 ps TOF would provide $\pi/K$ separation up to 7 GeV, which could potentially provide all of the lower momentum coverage for a gaseous RICH. Going even further in rapidity, the momentum of the very forward particles, which have a long flight path near the beam pipe and are hard to measure using a magnetic spectrometer, could also be provided by TOF.

TOF systems require a start-time, which could be provided by measuring the event vertex location along the beam line. The ultimate limitation here is the length of the electron bunch, which is e.g. ~5 mm in the eRHIC design, translating into ~15 ps timing uncertainty. For events with two and more tracks the start time can also be self-determined by iterative Bayesian techniques on the track timing information itself. However this basically requires $4\pi$ acceptance coverage by high-resolution timing detectors, which can become prohibitively expensive.

It should be noted that some timing is always required at the EIC in order to associate the particle track with a specific bunch, since each bunch has particular properties such as the polarization. However, in the currently envisioned EIC accelerator scenarios the bunch separations are relatively large (500 ps and ~9 ns in JLAB and BNL implementations, respectively), requiring only modest timing resolution for these purposes.

#### 4.3.3.5 Transition Radiation Detector (TRD)

Transition radiation (TR) is emitted when a relativistic charged particle crosses the boundary between two media of a radiator with different dielectric constants [35]. The number of TR photons and the total transition radiation energy emitted are proportional to the $\gamma$ factor ($\gamma = E/m$) of the charged particle [36]. Due to the large mass difference between electrons and hadrons, transition radiation detectors could be used for $e/\pi$ separation and can provide rejection factor of about 10-1000 [37] in the momentum range 2-100 GeV/$c$ for a relatively small detector volume.

Typically, a material with a large number of boundaries is used as a TR radiator. For example, a stack of regularly spaced Mylar foils separated by air gaps, or something with irregular boundaries such as foam or fleece material. The typical radiator thickness is about ~0.15% $X_0$ for a 1 cm of material. Due to the very small TR emission angle, the TR signal in a detector is overlapping with the charged particle ionization ($dE/dx$). Different methods and technology choices exist for TR identification and $dE/dx$ separation.

Traditionally, MWPCs and straw tubes filled with Xe-based mixtures, needed to improve detection efficiency for TR photons, have been used within various accelerator based experiments, but a GEM tracker should also work, and respective project exists within the scope of the EIC Detector R&D program.

#### 4.3.3.6 Hadron-Blind Detector (HBD)

The HBD is a threshold Cherenkov detector with $CF_4$ gas and a very special layout of the GEM readout, which can perform e/π identification from low momenta up to about 4 GeV/$c$, where it only produces signals for electrons, but not for hadrons. In the original PHENIX HBD, the readout was located on the barrel. Since the gas is the same as the one that would be used in a TPC, the HBD functionality can in principle be combined with a TPC with longitudinal drift, which has its readout on the endcaps. Aside from cost and complexity, there would be no downside to having such an additional capability in the TPC. The momentum range covered by the HBD would also be ideal for the electron-going endcap. Building an HBD with the readout on the endcaps of the cylinder rather than in the barrel would in principle be easier but would require more than 0.5 m of space in the EIC detector, dedicated to HBD. It could also be possible to combine this with a radial TPC (rTPC) readout, which would add tracking functionality. However, while small rTPCs have been used successfully in solenoidal (longitudinal) magnetic fields, it is not clear how well such a device would perform if the drift radius was of the size of the endcap tracker. Thus, while such a device could potentially be very interesting for an EIC, a significant amount of R&D would be needed to demonstrate its feasibility and performance.

#### 4.3.3.7 Photosensors and Electronics

While not a detector system *per se*, photosensors and electronics are essential for reaching the cost and performance goals of all the EIC PID subsystems. The consideration of possible photo-sensor solutions for each detector component is driven by the operational parameters of the detector, with cost optimization in mind. The photosensor requirements of a selection of PID subsystems are listed in the table below. In particular, small pixels with individual readout, good timing even with small signals, and tolerance to high magnetic fields and radiation are essential. Thus, these are the important R&D items, both during the development phase of the detectors described above, as well as for their final implementation.

Photomultipliers (PMTs) that are viable candidates for EIC applications are Silicon PMs (SiPMs), Multi-anode PMTs (MaPMTs), commercial Microchannel-Plate PMTs (MCP-PMTs), Large-Area Picosecond Photodetectors (LAPPDs), and Gaseous Electron Multipliers (GEMs) - the latter for a gas-only RICH.

| **Parameter** | **DIRC** | **mRICH, dRICH** |
|---|---|---|
| Gain | ~106 | ~106 |
| Timing resolution | ≤ 100 ps | ≤ 800 ps |
| Pixel size | 2-3 mm | ≤3 mm |
| Dark noise | ≤ 1 kHz/cm2 | ≤ 5 MHz/cm2 |
| Radiation hardness | Yes | Yes |
| Single-photon mode operation | Yes | Yes |
| Magnetic-field tolerance | Yes (1.5–3 T) | Yes (1.5–3 T) |
| Photon detection efficiency | ≥ 20% | ≥ 20% |

*Table 6. Photo-sensor requirements for various types of EIC Cherenkov detectors*

As seen in Table 6, this group of Cherenkov detectors share similar requirements, and it would eventually be possible to use common photo-sensors and electronics, reducing development and procurement costs. The main difference is that the DIRC requires not only small pixel size, but also fast timing and low dark count rate (DCR). Such timing resolution is satisfied by currently available MCP-PMTs (including LAPPDs), but the electronics would also have to provide this capability, even for small signals. The DCR requirement currently precludes the use of SiPMs for the DIRC, but this may become possible in the future as sensors performance improves. Radiation hardness is also important for all photosensors, but in particular for the ones located near the beam line. This would not be a good location for SiPMs, although they can be used in other locations where their magnetic-field tolerance is beneficial. Since the photo-sensors are also the main cost driver for the mRICH and dRICH, sensor cost reductions would have a large impact on the overall system cost.

Development of GEM-based photo-sensors is also important. Improvement of the performance in the UV is useful for the gas-only RICH. And although it would be an ambitious undertaking, if a photocathode was available that would be sensitive in the visible region, it could provide a low-cost, radiation-hard alternative to the more traditional photosensors.

## 4.4 Luminosity Measurements

Essential to any physics program at an EIC is the precise measurements of the delivered luminosity, better than 1%. The measurement of the luminosity at the collision energies under consideration can be based on measuring bremsstrahlung photons from the *ep*-scattering, $ep \rightarrow ep\gamma$ . This is a well-known calculable QED process with a large cross-section making it a prime candidate to measure the luminosity. Additionally, the radiative corrections in the relevant energy range are small. This reaction produces photons that are emitted in a narrow cone around the direction of the incoming electron beam, and so the goal for this measurement is to measure photons in the very backward region. This can be seen in *Figure 23*, which plots the analytic calculation from QED for the differential cross section as a function of photon energy (left) and polar scattering angle (right) for different beam energy configurations.

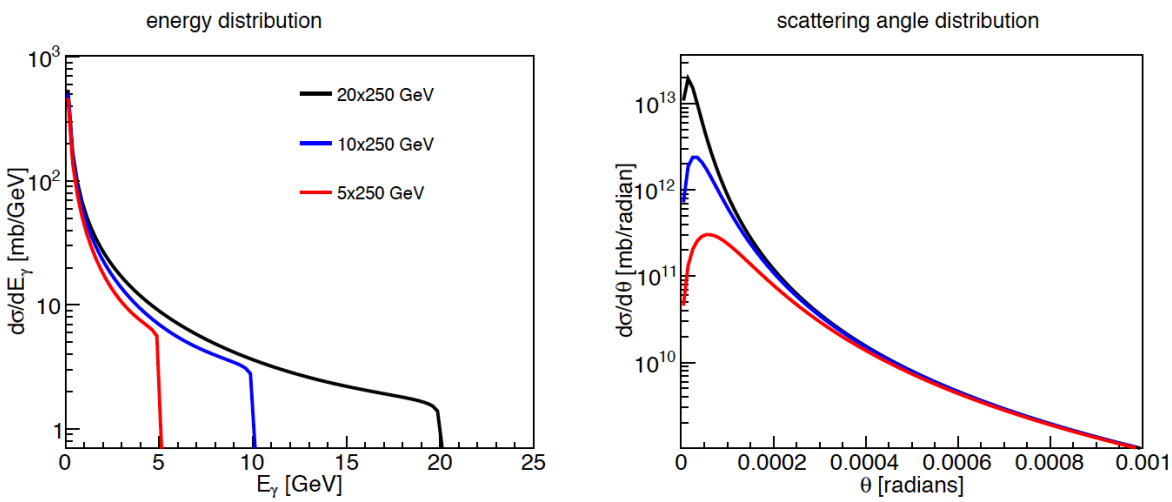


*Figure 23 The differential cross section for Bethe-Heitler scattering as a function of photon energy (left) and scattering angle (right). Different collision energies are shown by the color-coding and described in the legend.*

As can be observed in *Figure 23*, photons from this process generally scatter at small angle, where the peak of the distribution is around 0.03 mrad. Thus, the spread of the cone of photons in the detector will be dominated by beam effects, such as the angular divergence that is typically a factor of 10 or so larger than that from direct physics process. The angular divergence quantifies the spread in the angle at which the collision occurs. Typically beams at the IP are squeezed to drive up the luminosity.

The luminosity is directly related to the number of detected photons as $\mathcal{L} = N_\gamma/(A\sigma)$ , where $\mathcal{L}$ is the luminosity, $N_\gamma$ is the number of detected photons, $A$ is the acceptance correction for photons in the measured range, and $\sigma$ is the integrated cross-section in the measured range. Since the cross section is accurately known, the main sources of system-

atic uncertainty are on $N_\gamma$, the number of photons that we measure coming directly from the elastic *ep*-scattering, and the acceptance correction.

The main requirement of the luminosity measuring system is to have sufficient acceptance through the machine to the detectors. This is not a trivial task and requires close collaboration with the machine designers. The detectors need to be fairly radiation hard because of to the large luminosity and high intensity of Bethe-Heitler photons. It is important to reduce synchrotron radiation flux hitting the detector. The detector also needs to be able to track the luminosity as a function of time, so that changes in luminosity over each fill can be accounted for.

## 4.5 Trigger and Data Acquisition

MISSING

- Streaming vs. triggered
- RO Electronics (what is needed what might exist)
- Where is R&D needed?

## 4.6 Polarization Measurements

### 4.6.1 Electron Beam

Systems need to be in place to quantify the polarization of the beam. Depending on the specifics of the electron beam of the machine, the polarization needs to be monitored as a function of time and per bunch. If one invests in an injection scheme that requires multiple cathodes to fill the machine, the polarization monitoring must be done for each individual cathode as a function of time. The natural option for electron beam polarization measurements at the energy and current of the beams under consideration is Compton scattering.

Under this method, circularly polarized laser light impinges upon the electron beam. The cross section of the Compton interaction depends on the polarization of the photon and electron. Since this is a pure QED process, it can be calculated analytically, giving a functional form for the asymmetry in the cross section between the polarization combinations in the collisions. The asymmetry can be measured by counting the photons produced with collisions with the different spin combinations, with the results being fit to the analytical expression for the asymmetry. The polarization is a fit parameter, and thus can be extracted from the measurement. The main requirement for such a measurement is to have a space for a Compton interaction point, where the laser hits the beam. This process must also be parasitic to the beam in that the measurement needs to have no effect on the beam. And the rate of collisions must be sufficiently high to obtain polarization measurements on the time scale of seconds or minutes. A high rate is also required to minimize systematic uncertainties to the sub-percent level.

### 4.6.2 Proton Beam

MISSING

### 4.6.3 Light Ion Beams

MISSING

# 5 The EIC R&D Program

In January 2011 Brookhaven National Laboratory, in association with Jefferson Lab and the DOE Office of Nuclear Physics, announced a generic detector R&D program to address the scientific requirements for measurements at a future EIC. The primary goals of this program are to develop detector concepts and technologies that have particular importance for experiments in an EIC environment, and to help ensure that the techniques and resources for implementing these technologies are well established within the EIC user community. It is also anticipated that the topical detector-type-oriented "consortia" (calorimetry, tracking, PID and others) will partly form a basis of the active EIC community and later on participate in shaping up the actual EIC physics collaboration(s).

This program is supported through R&D funds provided to BNL by the DOE Office of Nuclear Physics. It is not intended to be specific to any proposed EIC site, and is open to all segments of the EIC community. Proposals should be aimed at optimizing detection capability to enhance the scientific reach of polarized electron-proton and electron-ion collisions up to center-of-mass energies of 50-200 GeV and *ep* equivalent luminosities up to a few times $10^{34}$ $cm^{-2}$ $s^{-1}$. Funded proposals are selected on the basis of peer review by a standing EIC Detector Advisory Committee consisting of internationally recognized experts in detector technology and collider physics. This committee meets twice per year, to hear and evaluate new proposals, and to monitor progress of the ongoing projects. The program is administered by the BNL Physics Department. This program is funded at an annual level of ~$1.0M, subject to availability of funds from DOE NP.

The following projects were or are supported by the program:

| ID | Topic | Status |
|---|---|---|
| RD 2011-1 | Fiber Sampling Calorimeters | Merged into eRD1 consortium |
| RD 2011-3 | DIRC -based PID | Merged into eRD14 consortium |
| RD 2011-5 | Radiation resistant Si PM | Concluded |
| RD 2011-6 | Tracking/PID/Simulation | Merged into eRD6 consortium |
| RD 2012-3 | Forward Tracking: GEM & Micromegas | Renamed into eRD3 |
| RD 2012-5 | Physics Simulations/Physics Event Generators | Concluded |
| RD 2012-8 | Crystal R&D for a forward calorimeter | Concluded |
| RD 2012-11 | Spin-light polarimeter | Concluded |

| | | |
|---|---|---|
| RD 2012-12 | Forward RICH detector | Merged into eRD14 consortium |
| RD 2012-13 | Forward EM pre-shower | Concluded |
| RD 2012-14 | Tungsten fiber Calorimeters | Merged into eRD1 consortium |
| RD 2012-15 | GEM based TRD | Concluded |
| RD 2013-2 | Magnetic field cloaking device | Renamed to eRD2 |
| RD 2013-5 | 10 Picosecond TOF: MCP-PMTs | Merged into eRD14 consortium |
| RD 2013-6 | Polarimetry & luminosity monitor | Renamed to eRD12 |
| eRD1 | EIC Calorimeter Development | Calorimeter consortia, ongoing |
| eRD2 | A Compact Magnetic Field Cloaking Device | Concluded |
| eRD3 | Design and assembly of fast and lightweight barrel and forward tracking prototype systems for an EIC | Merged with eRD6 |
| eRD6 | Tracking/PID | Tracking consortium, ongoing |
| eRD12 | Polarimeter, Luminosity Monitor and Low $Q^2$-Tagger for Electron Beam | Concluded |
| eRD11 | RICH detector for the EIC'S forward region particle identification | Merged into eRD14, ongoing |
| eRD10 | R&D Proposal for (Sub) 10 Picosecond Timing Detectors at the EIC | Merged into eRD14, ongoing |
| eRD14 | Proposal for an integrated program of Particle Identification (PID) challenges and opportunities for a future Electron Ion Collider (EIC) | PID consortium, ongoing |
| eRD15 | A proposal for Compton Electron Detector R&D | Ongoing |
| eRD16 | Forward/Backward Tracking at EIC using MAPS Detectors | Ongoing |
| eRD17 | DPMJetHybrid 2.0: A Tool to Refine Detector Requirements for *e*A Collisions in the Nuclear Shadowing/Saturation Regime | Ongoing |
| eRD18 | Precision Central Silicon Tracking & Vertexing for the EIC | Ongoing |
| eRD20 | Developing Simulation and Analysis Tools for the EIC | Ongoing |
| eRD21 | EIC Background Studies and the Impact on the IR and Detector design | Ongoing |
| eRD22 | GEM based Transition Radiation Tracker R&D for EIC | Ongoing |
| eRD23 | Streaming Readout | Ongoing |

*Table 7: List of past and ongoing R&D projects.*

Proposals, progress reports, presentations, and the committee reports can be found on the following web site: https://wiki.bnl.gov/conferences/index.php/EIC_R%25D

# References


[1] D. Boer et al., A report on the joint BNL/INT/Jlab program on the science case for an Electron-Ion Collider, arXiv: 1108.1713.

[2] A. Accardi et al., Electron Ion Collider: The Next QCD Frontier - Understanding the glue that binds us all,'', arXiv:1212.1701 [nucl-ex].

[3] F. Jacquet and A. Blondel, DESY 79/48 (1979), in Proceedings of the Study of an ep Facility for Europe, U. Amaldi (ed.).

[4] S. Bentvelsen, J. Engelen and P. Kooijman, in: W. Buchmüller and G. Ingelman (eds.), Proceedings of the Workshop on Physics at HERA, Oct. 29-30, 1991, Hamburg (DESY, Hamburg, 1992), Vol. 1, p. 23.

[5] T. Toll and T. Ullrich, Phys. Rev. C 87, 024913 (2013) and Comput. Phys.Commun. 185 (2014) 1835-1853.

[6] L. Zheng, E.C. Aschenauer and J.H. Lee; Determination of electron-nucleus collision geometry with forward neutrons, Eur. Phys. J. A50 (2014) no.12, 189, arXiv:1707.8055

[7] O.Tsai et al; Development of a forward calorimeter system for the STAR experiment, J.Phys.Conf.Ser. 587 (2015) no.1, 012053

[8] L. Serin, The ATLAS High Granular Timing Detector for the phase II Upgrade, CERN detector seminar, https://indico.cern.ch/event/731927/, June 2018.

[9] I. Valin et al, A reticle size CMOS pixel sensor dedicated to the STAR HFT, 2012 JINST 7 C01102

[10] Technical Design Report for the Upgrade of the ALICE Inner Tracking System, J. Phys. G 41 (2014) 087002, https://cds.cern.ch/record/1625842?ln=en.

[11] N. Wermes, CMOS detectors development, RD50 meeting, https://indico.cern.ch/event/719814/contributions/3022652/ , June 2018.

[12] W. Snoeys et al, A process modification for CMOS monolithic active pixel sensors for enhanced depletion, timing performance and radiation tolerance, NIMA 871 (2017) 90-96.

[13] T. Hemperek, Exploration of advanced CMOS technologies for new pixel detector concepts in High Energy Physics, PhD thesis, http://hss.ulb.uni-bonn.de/2018/5035/5035.pdf, March 2018.

[14] I. Peric et al, The FEI3 readout chip for the ATLAS pixel detector, Nucl. Instrum. Meth. A 565 (2006) 178.

[15] T. Kugathasan et al, Monolithic Pixel Development in a 180 nm CMOS for the outer pixel layers in the ATLAS experiment, TWEPP 2017, https://indico.cern.ch/event/608587/contributions/2614081/attachments/1523908/2381891/Monolithic_ATLAS_CERN_TWEPP_2017_TK_v1.pdf, September 2017.

[16] I. Berdalovic et al, Monolithic Pixel Development in TowerJazz 180 nm CMOS for the outer pixel layers in the ATLAS experiment, PSD 2017, https://indico.cern.ch/event/615961/contributions/2659613/attachments/1519758/2373597/Berdalovic_PSD11.pdf, September 2017.

[17] T. Wang et al, Depleted fully monolithic CMOS pixel detectors using a column based readout architecture for the ATLAS Inner Tracker upgrade, 2018 JINST 13 C03039.

[18] I. Peric, ATLASPix and MuPix8 in aH18, AIDA WP6 meeting, https://indico.cern.ch/event/666202/contributions/2722295/attachments/1525120/2384448/KIT_ATLASPix_and_MuPix8_in_aH18.pdf, September 2017.

[19] M. Kubantsev, "Performance of the PrimEx electromagnetic calorimeter", AIP Conf. Proc. 867 (2006) 51.

[20] A. Alavi-Harati et al., Phys. Rev. Lett. 83 (1999) 22.

[21] D. Boutigny et al., The BaBar Technical Design Report (SLAC-R-457).

[22] A. Abashian et al., Nucl. Inst. Meth. A 479 (2002) 117

[23] CMS Collaboration, The Electromagnetic Calorimeter Project Technical Design Report (CERN/LHCC/97-33).

[24] M. Aleksa, M. Diemoz, "Discussion on the electromagnetic calorimeters of ATLAS and CMS", Nucl. Inst. Meth. A 732 (2013) 442.

[25] C. Bebek et al., Nucl. Inst. Meth. A 265 (1988) 258.

[26] M. Akrawy et al., Nucl. Inst. Meth. A 290 (1990) 76.

[27] G.D. Barr et al., CERN/SPSC/90-22, SPSC/P253 (1990).

[28] V. Fanti et al., Phys. Lett. B 465 (1999) 335.

[29] U. Behrens et al., Nucl. Inst. Meth. A 289 (1990) 115.

[30] L. Balka et al., Nucl. Inst. Meth. A 67 (1988) 272.

[31] M. Adinolfi et al., Nucl. Inst. Meth. A 482 (2002) 363.

[32] A. Antonelli et al., Nucl. Inst. Meth. A 354 (1995) 352.

[33] A. Decamp et al., Nucl. Inst. Meth. A 294 (1990) 121.

[34] B. Aubert et al., Liquid Argon Calorimetry with LHC Performance Specifications (CERN/DRDC/90-31).

[35] V.L. Ginzburg, I.M. Frank, "Radiation of a uniformly moving electron due to its transition from one medium into another" **,** JETP 16 (1945).

[36] V.L. Ginzburg, V.N. Tsytovich, "Transition Radiation and Transition Scattering", Inst. of Physics Publishing, Bristol, 1990.

[37] A. Andronic, J.P. Wessels "Transition Radiation Detectors", 10.1016/j.nima.2011.09.041.

*Technical notes:*

- *References are handled as Endnotes (see Footnote menu) and then cross-referenced. The superscript cross-reference is change from* $^{NN}$ *to [NN] by hand.*
- *Figures with 2 or more plots should be setup and formatted via tables.*
- *Default font is Minion Pro.*

*Version History:*
*v1.0: Initial Release – October 19, 2018*